

# Calibration and Characterization of the Radiation Assessment Detector (RAD) on Curiosity

C. Zeitlin<sup>1,2</sup> · D.M. Hassler<sup>3</sup> · R.F. Wimmer-Schweingruber<sup>4</sup> · B. Ehresmann<sup>3</sup> · J. Appel<sup>4</sup> · T. Berger<sup>5</sup> · E. Böhm<sup>4</sup> · S. Böttcher<sup>4</sup> · D.E. Brinza<sup>6</sup> · S. Burmeister<sup>4</sup> · J. Guo<sup>4</sup> · J. Köhler<sup>4</sup> · H. Lohf<sup>4</sup> · C. Martin<sup>4</sup> · D. Matthiä<sup>5</sup> · A. Posner<sup>6,7</sup> · S. Rafkin<sup>3</sup> · G. Reitz<sup>5</sup> · Y.D. Tyler<sup>8</sup> · M. Vincent<sup>3</sup> · G. Weigle<sup>9</sup> · Y. Iwata<sup>10</sup> · H. Kitamura<sup>10</sup> · T. Murakami<sup>10</sup>

Received: 2 March 2016 / Accepted: 15 October 2016 / Published online: 2 November 2016  
© Springer Science+Business Media Dordrecht 2016

**Abstract** The Radiation Assessment Detector, RAD, is one of the ten instruments that make up the science payload of the Mars Science Laboratory Curiosity rover. RAD is an energetic particle detector, capable of measuring the charged and neutral particles that make significant contributions to the radiation dose that will be received by future human explorers when they visit Mars. Prior to the launch of MSL in November 2011, RAD and its near-identical twin flight spare unit were calibrated using laboratory sources, charged particle beams, and neutron fields. The initial calibration parameters obtained in these tests were used for real-time data analysis by the instrument's onboard software. These parameters have subsequently been refined using data obtained during the cruise to Mars and during Curiosity's mission on the surface of Mars. The most critical use of calibration is in the dosimetry analysis performed onboard. Calibration is also used in onboard analysis to determine which events should be stored for telemetry to Earth. Accelerator data obtained with the flight spare unit after Curiosity was launched provide detailed information about the response of the organic and inorganic scintillators to ion beams over a wide range of charge and energy. Here we report on the methods used to determine calibration parameters, the

---

✉ C. Zeitlin  
[cary.j.zeitlin@nasa.gov](mailto:cary.j.zeitlin@nasa.gov)

- <sup>1</sup> Lockheed Martin Information Systems & Global Solutions, Houston, TX, USA
- <sup>2</sup> Southwest Research Institute, Earth, Oceans and Space, Durham, NH, USA
- <sup>3</sup> Southwest Research Institute, Boulder, CO, USA
- <sup>4</sup> Christian Albrechts University, Kiel, Germany
- <sup>5</sup> German Aerospace Agency, Cologne, Germany
- <sup>6</sup> California Institute Technology, Jet Propulsion Laboratory, Pasadena, CA, USA
- <sup>7</sup> NASA Headquarters, Washington, DC, USA
- <sup>8</sup> Southwest Research Institute, San Antonio, TX, USA
- <sup>9</sup> Big Head Endian LLC, Burden, KS, USA
- <sup>10</sup> National Institute of Radiological Science, Chiba, Japan

results obtained, as well as providing an overview of the modifications to the instrument's software and configuration that have been made over the course of the mission.

**Keywords** Mars · Energetic particle radiation · Galactic cosmic rays · Solar particle events · Curiosity rover · Space radiation dosimetry

## 1 Introduction

The Radiation Assessment Detector, RAD, has been previously described in detail in the literature (Hassler et al. 2012). Several publications (Zeitlin et al. 2013; Hassler et al. 2014; Köhler et al. 2014, 2015; Ehresmann et al. 2014; Rafkin et al. 2014; Posner et al. 2013; Guo et al. 2015a, 2015b; Wimmer-Schweingruber et al. 2015) have described the results obtained since the launch of the Mars Science Laboratory in November 2011. Preliminary calibration of the instrument was described in Hassler et al. (2012); updated and expanded information is presented here. Table 1 defines several acronyms and other terms used in the following. Calibration as defined here encompasses several aspects that mirror the internal complexity of the instrument. First and most importantly, it refers to the conversion of digitized pulse heights to energy deposited values, i.e., energy calibration. In addition, we consider other important aspects: trigger threshold settings, dose-rate calibration, and event selection criteria used in the onboard data processing. We also present a condensed history of the (mostly small) adjustments that have been made to flight parameters and software over the course of the mission to date.

RAD is the first energetic particle detector to make measurements on the surface of another planet. It is designed to measure the particles, both charged and neutral, that are relevant for protection of future human explorers. The charged particles of interest are Galactic Cosmic Rays (GCRs) and occasional Solar Energetic Particles (SEPs). Interactions of these particles in the atmosphere (about  $22 \text{ g cm}^{-2}$  column depth in Gale Crater on average) and in the regolith result in a complex radiation field on the surface of Mars. The particles measured by RAD include background from the radioisotope thermoelectric generator (RTG) that powers Curiosity; these contributions must be separated from the naturally-occurring Martian radiation environment.

While most of the radiation dose and dose equivalent are due to charged particles, neutral particles are also of considerable interest. Because they are all secondary particles, neutral-particle spectra allow for detailed comparisons of data with predictions of radiation transport models that are vitally important for planning future exploration missions. The high-energy neutrons and  $\gamma$ -rays that RAD measures are not distinguishable from one another on an event-by-event basis, but the energy spectra have been successfully separated on a statistical basis (Köhler et al. 2011, 2014, 2015).

## 2 Instrument Overview

Here we briefly recap the instrument description in Hassler et al. (2012). The RAD instrument consists of the sensor head (RSH) and electronics box (REB). The RSH contains the detectors and front-end electronics (FEE). Seventeen analog signals are generated in reverse-biased silicon diodes in the RSH, from which charge is collected and amplified by charge-sensitive preamplifiers and first-stage shaping amplifiers. Figure 1 illustrates the

**Table 1** Definitions and acronyms

Term or acronym	Meaning	Comments
$\Delta E$	$dE/dx$ integrated over a finite $dx$	Deposited energy.
ADC counts	Output of Analog to Digital Converter	RAD has a 14-bit ADC; output values in the range from 0 to 16383 are possible.
$dE/dx$	Average energy lost by a charged particle per unit distance.	In thin detectors such as the RAD A, B, and C silicon detectors, $dE/dx$ is nearly constant in the large majority of cases.
EVIL	Electronics for VIRENA Logic	Table with calibration and other parameters used by L2.
FEE	Front-end electronics	RAD's front-end electronics are located adjacent to the detectors and consist of preamplifiers and first-stage shapers.
FSW	Flight software	Currently on version 2.7 as of this writing.
Gain (G)	ADC counts per unit $\Delta E$ .	Onboard, $1/G$ is used in calculations.
L2	Level 2	Firmware module that resides in the FPGA on the RAE board.
L3	Level 3	Firmware module that resides in the FPGA on the RDE board.
LET	Linear Energy Transfer	Usually refers to energy lost in an infinite volume, i.e., without regard to energetic electrons that may escape from finite detector volumes.
MIP	Minimum-Ionizing Particle	Highly relativistic particles with charge $Z = 1$ , e.g., protons, muons, electrons.
PHA data	Pulse Height Analysis event records.	Sparsified, compressed, list-mode readout of channels digitized in an event.
RAE	RAD Analog Electronics PC board	Includes VIRENA and associated FPGA.
RDE	RAD Digital Electronics PC board	Includes FPGA.
REB	RAD Electronics Box	Contains RAE, RDE, and RSE.
RSE	RAD Sleep Electronics PC board	Holds power supply and sleep circuit.
RSH	RAD Sensor Head	Contains detectors and FEE.
VIRENA	Voltage-Input Readout for Nuclear Applications	Custom ASIC in the REB with 36 channels, each with a shaping amplifier, linear amplifier, two comparators, and peak-hold circuit.

functionality of the RSH and the segmentation of the A, B, and C silicon diodes. The remaining signals come from diodes that are optically coupled to the scintillators D, E, and F. The D detector is made of CsI(Tl), while E and F are Bicron BC-432 plastic. Each analog output from the RSH is used as input to two redundant channels in the VIRENA ASIC, a custom 36-channel device manufactured by NOVA R&D. The channels and their nominal characteristics are listed in Table 2. The VIRENA has a large number of adjustable parameters, which are set in the “EVIL” table that is loaded at boot time. Each VIRENA channel contains a first-stage linear amplifier, a fast discriminator which uses the linear amplifier output directly, a second-stage shaping amplifier, and a slow discriminator that uses the output of the second-stage shaper. The latter output is also the input to a peak-hold circuit. A few

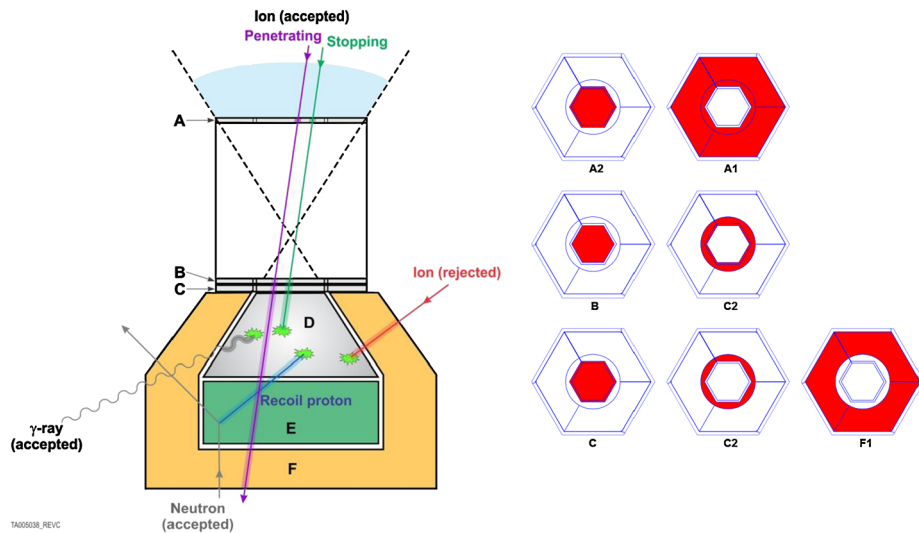


**Fig. 1** *Left:* Schematic representation of the RSH illustrating detection of important particle types. *Right:* Segmentation of the A, B, and C silicon diodes. Two charged particle coincidence triggers are defined, A1 • B and A2 • B. The outermost portion of the C diode is labeled F1 as it is optically coupled to the upper part of the F scintillator, and collects scintillation light from it. Segments of the B and C diodes are wired together to form the C2 channel, used as a veto in neutral particle analysis

channels (BU, DH, and EH) have their fast discriminators enabled; when any of these fires, the Level 2 (L2) trigger logic examines the “slow token mask” which consists of the bits (also referred to as “tokens”) that are set, or not, according to the slow discriminator outputs. Unlike the fast discriminators, all slow discriminators are enabled. The L2 logic looks for a match to any of 16 pre-defined bit patterns; if one or more matches are found, digitization of some or all signals on the peak-hold circuits follows. Table 3 lists the pre-defined L2 slow token patterns. The selection of channels to be digitized depends on which L2 pattern was matched; each of the pre-defined slow token patterns has an associated “readout mask” that in most cases limits the number of channels to be digitized to only those that are most relevant for the particular trigger type. For instance, if the slow token pattern match suggests that a neutral particle has been detected in the D detector (L2 trigger number 7), then only signals from D and the anticoincidence detectors are digitized. If multiple coincidence requirements are satisfied, the readout mask is the logical OR of the readout masks of the individual matches. Because the L2 triggers depend entirely on slow tokens, it is important that all slow thresholds are accurately set to the intended levels; this is an essential part of the overall calibration of the system. At the post-digitization stage, the calibration parameters (which are also specified via the EVIL table) come into effect, as described in Sect. 3 below.

Expected MIP signal levels at the VIRENA output are given in the far-right column of Table 2, including a factor of 0.6 that arises from a resistive divider circuit at the VIRENA input. Full scale on the 14-bit ADC (shared by all channels) is 0 to 2.0 V. The VIRENA baseline output is biased by a positive voltage, typically about 200 mV, with some channel-to-channel variation. This bias moves the pedestals (the ADC reading when there is no signal on the input) well above 0, which reduces the dynamic range by about 10 % but avoids using the low end of the ADC range where differential non-linearity can be a problem. In Table 2, the energy required to create an electron/hole pair in silicon is taken to be 3.6 eV.

**Table 2** Readout channel specifications

Channel label	Feedback capacitance (pF)	FEE shaper gain	VIRENA input gain (adjustable)	Overall relative gain	VIRENA output, V/MeV in Si	VIRENA output for MIPs (mV)
A1L, A2L, BL	8.2	$\times 1$	$\times 1$	$\times 0.12$	$3.0 \times 10^{-3}$	0.26
A1M, A2M, BM	8.2	$\times 1$	$\times 8$	$\times 1$	$2.6 \times 10^{-2}$	2.1
A1H*, A2H*, BH	8.2	$\times 16$	$\times 1$	$\times 2$	$5.2 \times 10^{-2}$	4.2
A1U, A2U, BU	8.2	$\times 16$	$\times 8$	$\times 16$	0.42	33
CL	3.3	$\times 1$	$\times 1$	$\times 0.3$	$8.1 \times 10^{-3}$	0.65
CM	3.3	$\times 1$	$\times 4$	$\times 1.2$	$3.2 \times 10^{-2}$	2.6
CH	3.3	$\times 8$	$\times 1$	$\times 2.4$	$6.5 \times 10^{-2}$	5.2
CU	3.3	$\times 8$	$\times 8$	$\times 19$	0.52	41
C2L	1	$\times 8$	$\times 1$	$\times 8$	0.21	17
C2H	1	$\times 8$	$\times 8$	$\times 64$	1.70	136
DL	8.2	$\times 1$	$\times 1$	$\times 0.12$	$1.7 \times 10^{-4}$	2.7
DN	8.2	$\times 1$	$\times 8$	$\times 1$	$1.4 \times 10^{-3}$	22
DM*	1	$\times 1$	$\times 1$	$\times 1$	$1.4 \times 10^{-3}$	22
DI	1	$\times 1$	$\times 8$	$\times 8$	$1.1 \times 10^{-2}$	178
DH	1	$\times 8$	$\times 1$	$\times 8$	$1.1 \times 10^{-2}$	178
DU*	1	$\times 8$	$\times 8$	$\times 64$	$9.1 \times 10^{-2}$	1421
EL	1	$\times 1$	$\times 1$	$\times 1$	$2.0 \times 10^{-4}$	0.74
EN	1	$\times 1$	$\times 8$	$\times 8$	$1.6 \times 10^{-3}$	5.9
EM*	1	$\times 4$	$\times 1$	$\times 4$	$8.2 \times 10^{-4}$	2.9
EI	1	$\times 4$	$\times 4$	$\times 16$	$3.3 \times 10^{-3}$	12
EH	1	$\times 16$	$\times 1$	$\times 16$	$3.3 \times 10^{-3}$	12
EU*	1	$\times 16$	$\times 8$	$\times 128$	$2.6 \times 10^{-2}$	94
F1L*, F2L*	1	$\times 16$	$\times 1$	$\times 16$	$3.3 \times 10^{-3}$	12
F1H, F2H	1	$\times 16$	$\times 8$	$\times 128$	$2.6 \times 10^{-2}$	94

Note: Channels marked with asterisks are not in the readout mask for any L2 matching trigger

The light output of the D scintillator (CsI) is taken to be 54000 photons/MeV,<sup>1</sup> as per the manufacturer's specification for light yield from  $\gamma$ -rays; the scintillation light is assumed to be divided equally among the three photodiodes that are optically coupled to the crystal. Similarly, the outputs of E and F are taken to be 8000 photons/MeV,<sup>2</sup> again as specified for  $\gamma$ -rays, and for E the light is again divided among three photodiodes. The assumed equal division of light among photodiodes for D and E is correct on average, but for any given particle entering a scintillator, the light sharing depends on the trajectory of the incident particle and on stochastic processes. For purposes of calculating expected signal levels, the quantum efficiency of the photodiodes is taken to be 0.8 based on the emission spectra and photodiode sensitivity curve.

<sup>1</sup>The data sheet is available on the manufacturer's web site: [http://www.crystals.saint-gobain.com/CsI\(Tl\)\\_scintillator.aspx](http://www.crystals.saint-gobain.com/CsI(Tl)_scintillator.aspx).

<sup>2</sup>The data sheet is available on the manufacturer's web site: [http://www.crystals.saint-gobain.com/Plastic\\_Scintillators.aspx](http://www.crystals.saint-gobain.com/Plastic_Scintillators.aspx).

**Table 3** L2 matching patterns

Event type	L2 trigger	Hits required	Not hit	Comments
Charged particle, outer FOV	0	A1U, BU	C2H	Low LET (sparse readout).
Charged particle, inner FOV	1	A2U, BU	C2H	Low LET (sparse readout).
Heavy ion, outer FOV	2	A1M, BM	–	High LET, high priority (readout all).
Heavy ion, inner FOV	3	A2M, BM	–	High LET, high priority (readout all).
B dosimetry	4	BU	–	Any $\Delta E$ in B. Read only B.
E dosimetry	5	EH, EI	–	Any $\Delta E$ in E. Read only E.
E neutral	6	EH, EI	BU, CU, C2L, C2H, F1, F2	Neutral particle with a/c veto. Read E and a/c channels. Changed sol 806 (UTC 12/11/2014 04:31).
E neutral	6	EH, EI, EM	BU, CU, C2L, C2H, F1, F2	Neutral particle with a/c veto. Read E and a/c channels. Adding EM allows us to increase L2(6) threshold without affecting E dosimetry trigger L2(5).
D neutral	7	DH, DI	BU, CU, C2L, C2H, F1, F2	Neutral particle with a/c veto. Read D and a/c channels.
D • E coincidence	8	EH, EI, DH, DI	BU, CU, C2L, C2H, F1, F2	Neutral particle with a/c veto, high priority. Read D, E, a/c.
D heavy ion	9	DL, DM		Large $\Delta E$ in D corresponding to heavy ions; high priority. Readout all.
Penetrating charged particle	10	F2H, EH, DH, CU		No readout, counter only.
Stopping charged particle	11	A1U, BU	C2H, F1H, F2H	No readout, counter only.
Charged particle in calorimeter only	12	DH, EH, F2H	A1U, A2U, BU, CU	Readout all. Allows determination of pedestals for B channels with little or no crosstalk.
Reserved	13	BU	F1H, F2H, DH, EH	No readout, counter only.
Diagnostic	14	None		Fast trigger with no slow tokens set; redefined sol 1089 (UTC 29/08/2015 23:10).
Radon	14	BM	A1M, A2M, CM	Record (and flag with high PHA storage priority) triggers that may come from decay of radon or its daughters.
Catchall	15	None		Counts all fast triggers, with or without a matching L2 trigger.

Notes: For most of cruise, L2(4) was defined by BH, with a significantly higher threshold than BU. For sols 522–806 (UTC 24/01/2014 09:49 to 12/11/2014 04:05), L2(8) required hits in EH, EI, and DU, which gave a lower effective threshold in D. The L2(9) trigger threshold was reduced to about 500 MeV on sol 815, corresponding to energy depositions from relativistic carbon ions; prior to that time, the threshold corresponded to relativistic oxygen ions. The L2(12) trigger was implemented starting at sol 275.5 (UTC 15/05/2013 15:22); prior to that time, it was undefined

Onboard processing of the data, which includes application of calibration parameters, is described in detail in the following section. RAD operates on an autonomous, configurable cadence. The instrument acquires data for a specified period of time (typically 16 minutes), then packages its data and stores it in non-volatile memory. After data are stored, RAD sleeps for a specified period (typically 30 seconds, equal to the duration of a single tick of the sleep timer) before rebooting and resuming the observing cycle. The stored data are referred to as observation packets; each contains header information, housekeeping data, counter data, histogram data, and event pulse-height records, all in compressed form. The default packet size is nominally 16384 bytes, but it can optionally be doubled to include additional pulse-height data. Doubling of the packet size was enabled on sol 992 of the surface mission (UTC 29/08/2015 23:10), mainly to increase the share of low-priority events that are telemetered to Earth.

### 3 Calibration and Onboard Event Analysis

When an L2 pattern match is found, pulse heights are digitized and the ADC data are piped to the associated L2 logic module for the initial steps of event analysis. First, the calibration parameters for each channel in the readout mask are applied to determine the energy deposit as determined by that channel. Next, energy readings from multiple channels are combined to create a “detector energy.” Several algorithms for combining channels can be invoked via the EVIL table; the two that are used in operations are described in Appendix A. The event data have an associated “hardware priority” bit, indicating low or high priority, and the data are sent from L2 to a corresponding FIFO buffer for analysis by the onboard Level 3 software. These buffers may become full if the L3 software is busy processing previous events. The hardware priority bit is set by the L2 matching trigger; only heavy-ion events and neutral particle events with a D•E coincidence (L2 triggers 2, 3, 8, and 9) are tagged as high priority at this level. In August 2015, L2 trigger 14 was re-purposed to act as a “radon” trigger. It is set on events with a large energy deposition in B, regardless of other detectors; this can occur when a radioactive atom decays in the vicinity of B, and releases an alpha particle that deposits several MeV of energy in B with no other energy deposited in RAD. Thus in principle RAD can detect the presence of radon gas in the Martian atmosphere, if it is present at a sufficiently high concentration. These triggers are assigned high hardware priority.

In both Level 2 and Level 3, the intent of the priority schemes is to guarantee that rare events with the greatest potential to do biological damage are fully processed (guaranteed by the hardware priority bit) and telemetered to Earth (guaranteed by the “storage priority” value described below). The scheme assumes that such high-priority events are infrequent, and this has been borne out in practice, as the high-priority buffer has not yet been observed to become full, so that 100 % of these events are successfully passed from L2 to L3 for processing. The low-priority buffer has occasionally filled up, most notably during SEP events seen during the transit to Mars, though in typical operations it does not. When the low-priority buffer is full, no digitization of pulse heights occurs. In order to account for events that are not analyzed due to the buffer filling, counters are kept for both events that are passed to L3 and those that are not digitized, so that any needed corrections can be applied in ground analysis.

In L3, four types of histograms are defined: dosimetry, neutral particles, stopping charged particles, and penetrating charged particles. Details are given in Appendix B and also in Table 12 of Hassler et al. (2012). All histograms make use of the per-detector calibrated energy

values that are calculated in L2. In all cases, separate histograms are kept for events with low and high hardware priorities, so that any corrections needed to compensate for events lost due to full FIFO can be applied. As will be explained in detail, accurate calibration is most important for purposes of the dosimetry histograms. In all other categories, the analysis algorithms are highly tolerant of errors in calibration, so that the large majority of the most interesting events are stored and telemetered to Earth for more complete analysis than can be performed onboard. Very small shares (typically  $< 1\%$ ) of the least-interesting events are also stored and telemetered.

Events are first entered into the appropriate dosimetry histograms if there are valid energy depositions in B and/or E, and then in subsequent processing are sorted into one of three categories: penetrating charged particle, stopping charged particle, or neutral particle. Within each category, event selection criteria (cuts) are applied so that only events with physically reasonable patterns of energy deposition throughout the stack are included. The cuts are based on slow tokens and energy values; the latter depend on the calibration applied in L2. For the most part, processing of events with low hardware priority (which comprise the large majority of events) relies on slow tokens, whereas processing of events with high hardware priority makes use of a combination of slow tokens and calibrated energy values. This distinction was motivated by the expectation that, on events in which one or more detectors have large energy deposits, the slow tokens may be rendered inaccurate by crosstalk, so that the analysis should not simply rely on those bits. For example, for an event with low hardware priority that matched the L2(0) trigger (A1U•BU with no hit in C2) or L2(1) trigger (A2U•BU with no hit in C2), the L3 logic requires only that slow tokens are set in C, D, E, and F2 in order to populate the penetrating-particle histogram. No valid penetrating particle event will fail this check.

Each event category except dosimetry has an associated two-dimensional histogram; in each such histogram, a “storage priority” is associated with every bin. These priorities correspond to event storage buffers in the observation packet; the storage priority assigned in L3 has two bits (values 0 through 3) and should not be confused with the hardware priority assigned in L2, which has only one bit. When an event passes the pertinent cuts for its category, the corresponding two-dimensional histogram is updated, again using calibrated values to determine the  $x$  and  $y$  bins. The histograms are designed to enable particle identification; examples can be found in Hassler et al. (2012) (Fig. 22) and Ehresmann et al. (2014) (Fig. A2). Cut values and other parameters used in L3 are specified by RAD’s Setup table. Histogram storage can be enabled or disabled in the Setup table, and to date, the stopping and penetrating charged particle histograms have not been stored, leaving room for more PHA data in the observation packet. The charged particle histograms are (to date) not stored in the observation packet, but are used to assign storage priorities.

In addition to applying event selection cuts, the L3 logic has a configurable “catchall” by which events with high hardware priority may be assigned a particular storage priority even if they fail cuts. Events with low hardware priority that fail cuts are assigned storage priority 0, the lowest possible, as are events that match only triggers defined for B and/or E dosimetry. As currently configured, events that match L2 triggers 2 or 3 (heavy ion in A1 • B or A2 • B) but fail selection cuts are assigned storage priority 3, as are events that match only L2 triggers 9 or 14. For events with the other high priority trigger, L2(8), the L3 logic applies cuts on the energies in the anticoincidence detectors, which can cause events to fail cuts and be assigned storage priority 0.

Detailed descriptions of all L3 histograms can be found in Appendix B. Because calibrated energy values are used in cuts and in determining which histogram bin a particular event should be placed, it might seem that incorrect calibration and/or poorly chosen cut



values could cause good events to be lost, or at least to be given improper storage priority (e.g., priority 0 if cuts are erroneously deemed to have been failed). However, as noted, cuts for events with low hardware priority depend mainly on slow tokens, which in turn depend on threshold settings rather than energy calibration. And events with high hardware priority either pass cuts or are stored anyway because of the catchall logic. In sum, then, we expect no losses in L3 of events with high hardware priority, and there will similarly be no losses of good events with low hardware priority provided that slow thresholds are set correctly. Incorrect assignment of storage priority can occur due to calibration errors, but because the histogram bins are logarithmic, small errors have little or no impact. For example, if a stopping proton deposits 60 MeV in RAD but is, due to calibration inaccuracy, mis-measured by 25 % as having deposited 75 MeV, the net effect is that the event is not entered into exactly the right bin of the histogram, but rather populates a neighboring bin (a shift of one bin in  $x$  with no change in  $y$ ). This has no practical consequences.

## 4 First-Principles Calculations

Because the physics of energy deposition and signal generation in the detectors that comprise the RSH is well understood, we can make educated guesses as to the signal levels produced in the RSH detectors and FEE. The behavior of the VIRENA is also known reasonably well, so that the end-to-end gain of any given channel is calculable from first principles. This knowledge was used to produce the far-right table (expected MIP energy depositions) in Table 2. In practice, it is not surprising to find modest deviations from calculated values, for several reasons. First and foremost, all the silicon detectors and photodiodes in the RSH are connected to charge-sensitive preamplifiers that employ small-value feedback capacitors, ranging from 1 to 8.2 pF. The gain in all cases is inversely proportional to the value of the feedback capacitor,  $C_f$ . With such small values, parasitic capacitances may add to  $C_f$  and alter gains. Also, the capacitors used in the RSH have specified precisions of  $\pm 0.25$  pF, which corresponds to relative accuracies ranging from  $\pm 3$  % for the largest-value feedback capacitors (8.2 pF) to  $\pm 25$  % for the smallest (1 pF). The resistors used in op-amps further downstream (including those in the VIRENA) also affect gain. Resistor precisions are better than those of the feedback capacitors, typically within  $\pm 1$  % of nominal, but as there are many in the signal path, their combined variations may contribute to deviations from nominal gains. For the scintillators, there are additional complications of light collection efficiency, signal timing, and non-linearity of light yield vs. energy deposition. The yield per unit energy deposited in scintillators is in general a function of the particle type and energy. Scintillator manufacturers typically specify light yields for  $\gamma$ -rays, for which there is no quenching; light yields per unit energy deposit are generally smaller for heavier particles. Another important factor for the CsI(Tl) crystal used as the D detector is that its light output includes a slow component with an average decay time comparable to the shaping time of the amplifiers in the RSH. In practice, this means that some of the scintillation light arrives at the photodiode after the formation of the output pulse, yielding smaller pulse heights than predicted from a simple calculation. Furthermore, the relative contributions of the fast and slow components of CsI are temperature dependent, and RAD experiences fairly wide temperature swings throughout the course of a Martian day (or “sol”, length 1.027 Earth days). The expected calibration is sufficiently complex that data with a variety of particle types at different energies are required, rather than relying on calculations. However, for the A, B, and C channels, we expect the actual calibration to be in reasonable agreement with predictions, because (1) the energy required to create an electron/hole pair is well known to be 3.6 eV, with temperature

dependence on the order of  $\pm 1\%$  in RAD's operating range (Mazziotta 2008), and (2) the response of the electronics is highly linear. The dominant uncertainty in the calculated gain is in the value of the preamplifier feedback capacitor, as mentioned above.

In addition to the gain of each channel, we also need to know its pedestal. With RAD's 14-bit ADC, the maximum ADC count is 16383, and the baseline of the VIRENA output is deliberately shifted to about one-tenth of full scale. Theoretically, then, pedestals would all be 1638 ADC counts, and in fact the average is close to this value, but op-amp input offsets and other effects cause variation from channel to channel. Actual values must therefore be obtained by examining events in which a particular channel was read out but had no signal. This was facilitated, prior to delivery of the instrument to NASA, by putting RAD into "streaming mode" and using a special L2 matching pattern designed to read out all channels on all events. Several years have elapsed since delivery, and the instrument cannot be run in streaming mode in flight, so particular L2 triggers (such as number 12) must be defined to enable studies of possible pedestal drift without using excessive bandwidth. Temperature variations may also affect pedestals slightly, as discussed in Appendix E.

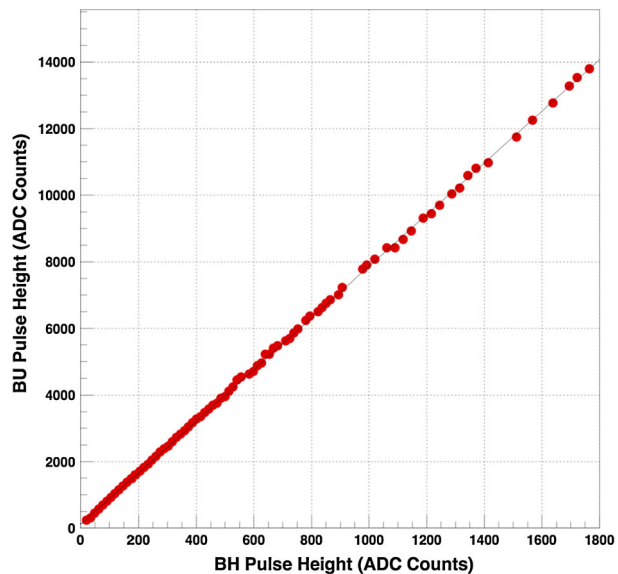
## 5 Preliminary Laboratory Calibration

Several beam tests with the flight RSH and an engineering model REB showed that the instrument performed as expected and had the required dynamic range capability. However, because the REB was not the flight model, these data were not used for the initial calibration. Instead, the flight unit was calibrated before delivery using the naturally-occurring flux of minimum-ionizing particles (MIPs), dominantly muons, that exists at the surface of the Earth, along with monoenergetic electrons (482, 554, 976, and 1048 keV) emitted from a  $^{207}\text{Bi}$  source. When an electron with energy in this range enters RAD in the  $A \bullet B$  field of view, several things can happen: it can undergo a large-angle scatter and lose all its energy in A; it can pass through A without significant scattering, depositing MIP-like energy, and lose its remaining energy in B; or it can pass through A and B without significant scattering, and lose its remaining energy in C. Electrons with energies of  $\sim 1$  MeV can also pass through C and penetrate into D, having deposited MIP-like energy in A, B, and C. In these cases, the signal in D is just above threshold and is not useful for calibration, nor do any of the electrons reach the E detector. Nonetheless, very useful calibration information can be obtained for A, B, and C using  $^{207}\text{Bi}$ . We used source data to determine gains for the high-gain (H and U) A1, A2, B, and C channels, all of which were found to be within  $\pm 10\%$  of values expected from first principles. (The interested reader can find the  $^{207}\text{Bi}$  spectra acquired by RAD in Fig. 15(a) of Hassler et al. 2012.) Initial calibration parameters for the D, E, and F channels were obtained with cosmic-ray muons. The appropriate values were stored in the initial flight EVIL table, and were updated soon after the first flight data arrived in December 2011, as described in the following section.

## 6 Bootstrap Calibration with Flight Data

MIPs, mostly GCR protons, are ubiquitous in space, and those that follow trajectories through the telescope defined by  $A \bullet B$  coincidences can be used for calibration with flight data. In particular,  $A2 \bullet B$  coincidence events provide a sample of MIPs that traverse D and E at small angles (less than  $18.4^\circ$ ) from the central axis of the detector.

**Fig. 2** Correlation between the average pulse height in the BU channel with the pulse height in the BH channel, for the region where the signals overlap. The two channels originate from the same point in the RSH, but go into separate VIRENA channels with different gains on their input amplifiers ( $\times 1$  and  $\times 8$ , respectively). The sparseness of points with large pulse heights is due to compression of the telemetered pulse-height data



It is important to note that for thin silicon detectors being traversed by high-energy charge-1 particles, there is a significant difference between the peak (most probable) energy deposition and the average as determined by the Bethe formula (Olive 2014; Bichsel 1988). The most probable  $\Delta E$  by a MIP at normal incidence through a 300  $\mu\text{m}$  silicon detector is 80 keV (Bichsel 1988), whereas the average energy deposition is about 117 keV. In flight data, we associate the MIP peak with the 80 keV value for A2  $\bullet$  B events rather than the larger, average value. For A1  $\bullet$  B events (used only to calibrate A1), a 5 % correction factor is applied to account for the longer average path length of particles that traverse the detector. MIP peaks are used to determine the gain factors for the highest-gain channels (“U” for A, B, and C; “H” and “I” for D and E). Gains of the other channels are determined by taking pulse-height ratios for the next lowest-gain channel, after pedestal subtraction. As an example, we show in Fig. 2 a plot of the average pulse height in the BU channel as a function of that in BH. A linear fit yields a ratio of 7.76, compared to the nominal value of 8.0 expected from the difference in VIRENA gains for the two channels. Since the gain of the BU channel is known from the MIP peak, the BH gain is simply scaled by this factor. In similar fashion, the gain of the BM channel is determined from a similar plot of BH vs. BM, and the gain of BL is determined from a plot of BM vs. BL.

Analysis of MIP peaks in early flight data resulted in several changes to the onboard calibration gain factors compared to the values that had been obtained on the ground. For A2 and B, changes were a few percent; other channels needed larger adjustments, but none was above about 10 %.

## 6.1 Energy Calibration Parameters

Table 4 shows the pedestal and inverse gain values as used in the EVIL table in use at the time of this writing, along with values based on the calculated gains in Table 2. The EVIL table inverse gain units are 2 keV/ADC count. As noted above, because the B and E detectors are used in the real-time calculations of doses in silicon and plastic, respectively, it is important

**Table 4** Calibration parameters

Channel	Pedestal	Inverse gain (2 keV/ADC)	Calculated inverse gain (2 keV/ADC)	Inverse gain/ calculated
A1U	1715	0.183	0.147	1.24
A1H	1777	1.30	1.17	1.11
A1M*	1850	2.41	2.35	1.03
A1L	2048	18.7	18.8	0.99
A2U	1629	0.161	0.147	1.10
A2H	1727	1.22	1.17	1.04
A2M*	2009	2.26	2.35	0.96
A2L	1636	17.3	18.8	0.92
BU	1644	0.154	0.147	1.05
BH	1784	1.25	1.17	1.07
BM	1978	2.28	2.35	0.97
BL	1570	17.7	18.8	0.94
CU	1891	0.102	0.118	0.86
CH	1779	0.827	0.945	0.88
CM	2042	1.98	1.89	1.05
CL	1743	7.70	7.56	1.02
C2H	1708	0.029	0.036	0.81
C2L	1622	0.229	0.286	0.80
DU*	1737	1.21	0.69	1.75
DH	1804	9.6	5.52	1.74
DI	1275	10.2	5.52	1.85
DM*	1940	93.9	44.2	2.12
DN	1899	94.8	45.3	2.09
DL	1865	738	362	2.04
EU*	1985	3.28	2.33	1.41
EH	1645	22.7	18.6	1.22
EI	1573	20.0	18.6	1.08
EM*	1858	80.8	74.5	1.08
EN	2008	46.9	37.3	1.26
EL	1817	417	298	1.40
F1H	1960	1.80	1.40	1.29
F2H	1795	1.82	1.40	1.30

Note: Channels are grouped by redundant pairs, e.g., A1U and A1H are the same physical channel in the RSH, input into two VIRENA channels as per Table 2. Channels marked with asterisks are not in the readout mask for any L2 matching trigger

that the readout channels for these detectors be calibrated as accurately as possible, and that we have good estimates of the calibration uncertainties. For all other channels, the system is tolerant of modest calibration errors, as explained in Sect. 3.

Observed gains of the silicon detector channels (A1, A2, B, and C) are, with a few exceptions, within  $\pm 10\%$  of the calculated values. A ratio greater than 1 indicates that the gain of the channel is smaller than expected; this can be due to parasitic capacitance in the

feedback loop, among other likely causes for these channels. For the scintillator channels, ratios are considerably larger, due to effects not accounted for in the calculation. For the D detector, the most important of these is the long time constant (3.5  $\mu\text{sec}$ ) associated with the slow component of the scintillation light. Given the 2  $\mu\text{sec}$  shaping time of the electronics, this means that a significant fraction of the scintillation photons do not contribute to the pulse, accounting for the (roughly) factor of two differences between measured and calculated gains for these channels. For the E and F detectors, observed signals are on the order of 30–40 % lower than expected from simple calculation, but that is based on the scintillation light yield from  $\gamma$ -rays, which is higher per unit energy deposit than from charged particles. This effect also contributes to the D detector channels having smaller gains than expected from naive calculations.

## 6.2 Non-linearity of D Light Output

The onboard calibration parameters used for all D, E, and F channels were determined from the energy deposition peaks for MIPs and the bootstrapping method described above. When MIPs traverse a scintillator, the light output is similar to that from  $\gamma$ -rays, but when particles of higher charge and/or lower energy deposit energy in a scintillator, the “calibrated” energy used in onboard processing will not necessarily be accurate. The non-linearity of light output from the scintillators is most significant for ions that stop in the detector and for heavy ions, though in both cases the effects are modest for the particle energies encountered in space. A valuable discussion of these effects can be found in an article by Koba et al. (2011), including a comparison of measured CsI(Tl) response to predictions from Birks’ formula (Birks 1964). This subject is discussed in detail in Appendix C.

The plots shown in Fig. 3 illustrate some of the complexity of the D detector calibration. Data from MSL’s surface mission (sols 1–600) are shown in the top two panels. The upper left panel of the figure, (a), shows data for penetrating particles with charges 1 and 2. In the panel on the upper right, (b), data are shown for particles with charge 1 that stopped in D. In both panels (a) and (b), the events were required to satisfy the A2 • B L2 trigger, and were selected based on energy deposition through the full telescope (A2, B, C, D, and E). Relatively high-energy ions were chosen in order to show well-separated clusters of charge 1 and 2 events. (The proton band overlaps the band of helium ions if the lower-energy protons are included.) The energy deposited in D is plotted on the y-axis, and the summed energy deposits in the A2, B, and C detectors is plotted on the x-axis. All energy deposits are calculated with the nominal calibration factors. In the panel (a), the most densely populated cluster, at lower left, is due to charge 1 particles, with a peak energy deposition in A2 + B + C of about 250 keV and 16 MeV in D, as expected for these particles. The fainter cluster of events centered at about 1.2 MeV on the x-axis and 70 MeV in D is due to relativistic helium ions; this cluster is also in the expected location, demonstrating that the energy scale in D is accurate for penetrating low-Z particles. In panel (b), the events in the lower-left corner, clustered most densely at low energies but with a tail going up to about 80 MeV deposited, are mostly due to electrons that stopped in D. (Some may be due to nuclear interactions of high-energy protons in D.) The band that begins at about 1 on the x-axis and 110 MeV on the y-axis and goes to about 9 MeV in x and 0 in y is due to stopping protons, labeled with the letter “p” in the figure. The fainter band above the proton band is from deuterons (labeled “d”), and an extremely faint band of tritons (labeled “t”) is also marginally visible, but here we are most interested in the proton band. Calculations show that the maximum energy that can be deposited by a proton in D is actually about 97 MeV for events that satisfy the A2 • B

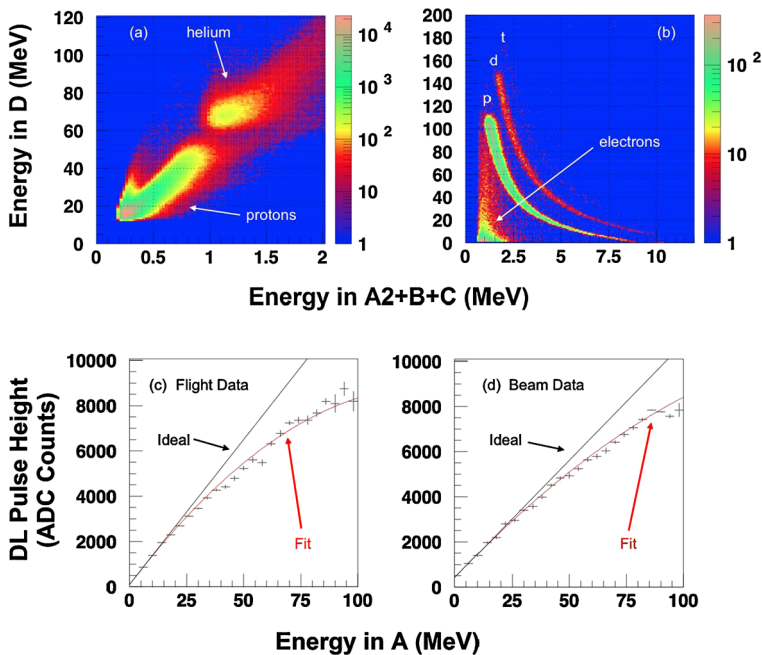


**Fig. 3** Energy depositions in D for penetrating and stopping particles. In panel (a) at the *upper left*, the energy deposited in D is plotted against the combined energy deposits in the A2, B, and C detectors for fully penetrating, high-energy protons and helium ions. In panel (b) at the *top right*, the same quantities are plotted for charge-1 particles that stopped in D, with evident bands for protons (p), deuterons (d), and tritons (t), along with a distinct cluster of events due to electrons. Panels (c) and (d) demonstrate the non-linear response of the light output from D for heavy ions. In both panels, the average pulse height in the low-gain readout channel of D is shown as a function of the energy deposited in the A detector, which has a highly linear response. The *black lines* in these panels represent the ideal case of no quenching, while the *red curves* are second-order polynomial fits to the data. The data in panel (c) were obtained in flight, whereas the data in panel (d) come from an accelerator run with 1 GeV/nuc  $^{56}\text{Fe}$  ions incident on RAD

coincidence, but the data show a maximum value of 110 MeV. The energy deposition scale is therefore off by about 15 % for stopping particles compared to the scale determined with penetrating particles. The deuteron band in the data extends to about 150 MeV, whereas calculations show that the maximum deposition from these particles in D is about 130 MeV. This behavior is consistent both with beam data and the results shown in Koba et al. (2011); see Appendix C for details. The onboard analysis software makes use of these (slightly incorrect) energy values, but for reasons described below, is highly tolerant of relatively small calibration errors such as these.

In panel (c) of Fig. 3, we show the average response of the D detector, specifically the DL channel, to heavy ions using data obtained on the surface of Mars. Data from both the A1 • B and A2 • B coincidences are combined in order to improve the statistics on relatively rare heavy ion events. The quantity plotted on the y axis is the average pulse height in the DL channel as a function of the energy in the A detector (larger of A1 and A2). The black line shows the extrapolated fit from the lowest few points, while the red curve is the best-fit second-order polynomial. The non-linear response of the light output is apparent. For 100 MeV deposited in A, the linear fit predicts a DL pulse height of about 13000 ADC counts, whereas the observed value is about 8000 ADC counts. Though this is a substantial

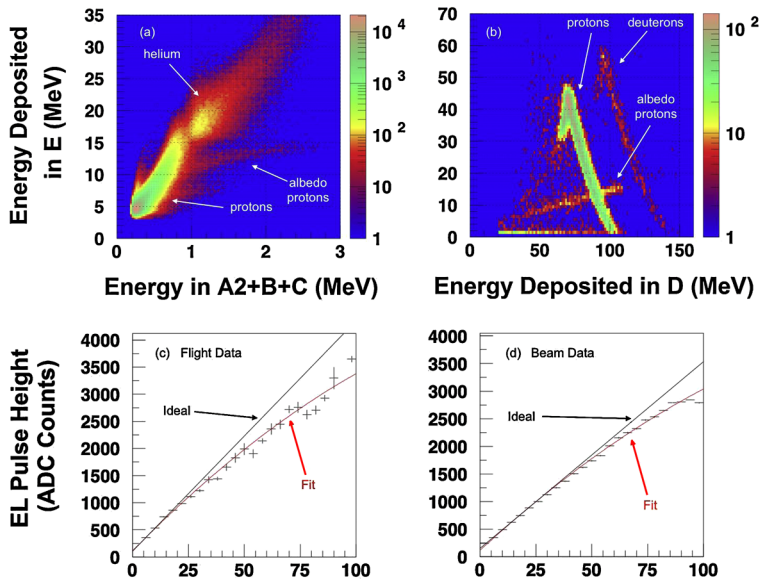


**Fig. 4** Energy depositions in E for penetrating and stopping particles. In panel (a) at the *upper left*, the energy deposited in E is plotted against the combined energy deposits in the A2, B, and C detectors for fully penetrating, high-energy protons and helium ions. In panel (b) at the *top right*, the same quantities are plotted for charge-1 particles that deposited no energy in F2, with evident bands for stopping protons and deuterons; a band due to albedo protons, which enter RAD from below, can also be seen. Panels (c) and (d) demonstrate the non-linear response of the light output from E for heavy ions. In both panels, the average pulse height in the low-gain readout channel of E is shown as a function of the energy deposited in the A detector. As in Fig. 3 above, the *black lines* in panels (c) and (d) represent the ideal case of no quenching, while the *red curves* are second-order polynomial fits to the data. The data in panel (c) were obtained in flight, whereas the data in panel (d) come from an accelerator run with 1 GeV/nuc  $^{56}\text{Fe}$  ions incident on RAD

difference, it is less than a factor of 2, and (as explained in Appendix B) it has no impact on the onboard data processing. The difference is also consistent with the observed behavior of the flight spare unit in high-energy heavy-ion beams. Panel (d) of Fig. 3 shows a similar plot obtained with a 1 GeV/nuc  $^{56}\text{Fe}$  beam at the Brookhaven National Laboratory (BNL). The quenching effect appears somewhat less severe in the beam data, possibly because the ions in that data set have, on average, higher energy than do those in the flight data.

### 6.3 Non-linearity of Light Output from E

In Fig. 4, we show plots for the E detector similar to those shown in Fig. 3 for D. The scatter plot in panel (a) shows energy deposition signals in E vs. the sum of A2, B, and C for penetrating charge 1 and charge 2 particles that fired the A2•B trigger. The main clusters are in the expected locations, as was the case for the corresponding D detector plots. The scatter plot in panel (b) shows the energy deposition in E vs. that in D for protons and deuterons that (mostly) stop in E, with energies based on the penetrating-particle calibration. Because E is thin compared to D ( $1.85 \text{ g cm}^{-2}$  vs.  $12.6 \text{ g cm}^{-2}$ ), relatively few particles stop in it, with a narrow range of energies. As can be seen in the figure, the event selection criteria used to make this figure included a cut requiring no discernable signal in F2—this evidently is not sufficient to guarantee stopping in E. However, the important point here is the maximum



energy deposition, which for E is about 46 MeV for particles in the A2 • B coincidence cone; the measured distribution extends to just above 50 MeV on this scale, an error of about 10 %, in the same direction as that seen for D. The maximum energy of stopping deuterons in E is about 63 MeV, but the deuteron band only extends to about 60 MeV on this scale.

Panel (c) of Fig. 4 shows the response of the EL channel to heavy ions observed on the surface of Mars. Again, the average scintillator response is plotted as a function of the energy in the A silicon detector. The quenching of these signals, as measured by the deviation from the straight-line fit to the data at small energy depositions, is noticeably less severe than that of the signal quenching in the D detector for a similar event sample. Panel (d) is similar to (c), again showing data obtained with the 1 GeV/nuc  $^{56}\text{Fe}$  beam at BNL. This shows even less quenching than the flight data, which is qualitatively the same effect seen in the comparable plots in Fig. 3; the reason is likely the same, i.e., signals are less quenched because beam ions are on average higher in energy than the ions measured on Mars.

## 6.4 Fast and Slow Threshold Settings

As mentioned above, among the fast triggers, only those for BU, DH, and EH are enabled. The rationale for using this subset is that the B fast trigger enables detection of A1 • B and A2 • B charged-particle coincidences, while the D and E fast triggers enable detection of neutral-particle events. Also, B and E fast triggers are needed for the L2 dosimetry triggers (4) and (5), respectively. In all cases, it is desirable to set the threshold as low as feasible while remaining above the electronic noise and, for D and E, above levels at which background from the RTG would dominate the trigger rate.

For charged particle detection, it is necessary to record MIPs, for which the most probable energy deposit in 300  $\mu\text{m}$  of silicon is 80 keV. The BU thresholds (both fast and slow) must be set no higher than 60 keV. Similarly, the A1U and A2U slow thresholds must also be at this level or below. In practice, the BU and A2U thresholds are set at about 30 keV as these segments are small in area (about 2  $\text{cm}^2$ ) and thus have small capacitances and low noise levels. However, A1 is relatively large in area (about 14  $\text{cm}^2$ ) and therefore has a comparatively high noise level; the A1U is accordingly set to 60 keV. It is notable that the ratio of A1U•BU to A2U•BU triggers has averaged 4.06 during the surface mission with little temporal variation. This is about 4 % different from the value of 4.23 that would be expected from the ratio of geometric factors for incident particles following an isotropic angular distribution. While this small difference could indicate a minor loss of particles in the A1U•BU viewing cone, the more likely explanation is that the incident particle distribution deviates slightly from perfect isotropy, as shown by detailed analysis (Wimmer-Schweingruber et al. 2015). This result is consistent with expectations for a lightly-shielded environment.

Concerns about the RTG background led us to set the D and E thresholds far above their respective noise levels prior to launch. D is a highly efficient  $\gamma$ -ray detector, so the readout system may be swamped with uninteresting background events if its threshold is too low. The D fast threshold is set to about 10 MeV, well above the energy of most  $\gamma$ -rays but below the 16 MeV expected  $\Delta E$  of a MIP traversing D vertically. The E slow thresholds have, over time, been adjusted to correspond to energy deposits smaller than the 3.6 MeV expected for a vertical MIP. However, the E fast threshold is around 6 MeV, which causes neutron detection efficiency to fall rapidly for incident energies below about 10 MeV. Table 5 lists current and initial threshold settings for the most important channels in the system, and



**Table 5** Fast and slow threshold settings

Channel	Current threshold energy	Current DAC setting	DAC setting at launch	Sensitivity (threshold change per DAC tick)	Relevant L2 matching patterns
BU Fast	33 keV	104	104	1.8 keV	
DH Fast	10.5 MeV	101	111	850 keV	
EH Fast	6 MeV	111	89	224 keV	
A1U Slow	60 keV	104	106	7 keV	0
A1M Slow	3 MeV	131	124	113 keV	2
A2U Slow	35 keV	93	93	3.5 keV	1
A2M Slow	3.2 MeV	143	123	113 keV	3
BU Slow	28 keV	90	90	3.5 keV	0, 1, 4
BH Slow	200 keV	119	119	14 keV	4, cruise only <sup>1</sup>
BM Slow	2.5 MeV	143	121	113 keV	2, 3, 14
DH Slow	9 MeV	118	123	420 keV	7, 8
DI Slow	9 MeV	87	111	420 keV	7, 8
DM Slow <sup>2</sup>	575 MeV	139	131	6.8 MeV	9
DN Slow <sup>3</sup>	320 MeV	186	131	3.5 MeV	9
DL Slow <sup>2</sup>	575 MeV	179	102	7 MeV	9
EH Slow	2.5 MeV	117	117	224 keV	5, 6, 8, 12
EI Slow	2.0 MeV	98	101	224 keV	5, 6, 8, 12
CU Slow <sup>4</sup>	25 keV	117	113	2.8 keV	6, 7, 8
C2H Slow <sup>4</sup>	100 keV	183	255	1.7 keV	0, 1
C2L Slow <sup>4</sup>	60 keV	119	95	3.4 keV	6, 7, 8
F1H Slow <sup>4</sup>	0.7 MeV	101	255	134 keV	6, 7, 8
F2H Slow <sup>4</sup>	0.7 MeV	99	142	34 keV	6, 7, 8

Notes:

<sup>1</sup>The L2(4) trigger definition was changed from requiring the BH slow token to the BU slow token at UTC 11/06/2012 17:34

<sup>2</sup>The L2(9) trigger was initially defined as a DN•DM slow token coincidence with a threshold of about 150 MeV

<sup>3</sup>At UTC 11/06/2012 17:34 the definition was changed to a DL•DM coincidence with a threshold of about 1100 MeV

<sup>4</sup>These slow tokens are used as veto signals (anticoincidence) for the L2 neutral particle triggers. The C2L slow token is also used as a veto for the L2(0) and L2(1) charged particle triggers to guarantee that particles are within the nominal viewing cone

the sensitivity of each to a change of one “tick” of the digital-to-analog converter (DAC) that controls the DC level to which signals are compared. The DACs have 8 bits, meaning that the maximum value is 255. Thresholds for the anticoincidence channels are special cases, and are discussed in Appendix D.

Adjustments to thresholds are made by changing the DAC setting via the EVIL table. The large majority of thresholds have either been stable since launch or have undergone only very minor changes. Some of the largest adjustments were made to the A1, A2, and B medium-gain channels used to define the high-priority heavy ions triggers L2(2) and L2(3).

## 6.5 Dose-Rate Calibration

No explicit calibration of the dose rates was performed prior to launch. Such tests are somewhat difficult to perform. RAD and similar flight instruments are designed to run at relatively low rates, a few hundred Hertz or less. Dose calibration requires accurate knowledge of the dose being delivered to the detector, and at typical facilities that information is only available using dosimetry systems such as ionization chambers that are designed for event rates that are orders of magnitude higher. This problem can be worked around, for example by using a plastic scintillator to count incident beam particles, at the cost of introducing extra mass on the beamline. A further complication for RAD calibration is that a highly parallel and spatially uniform beam broad enough to fully illuminate the E detector is required, and if one uses a heavy ion beam, the ions will traverse variable-length paths through the tapered profile of D on the way to E. The resulting dose rate in E can therefore be difficult to interpret due to fragmentation of the beam ions in D. However, it is straightforward to compare the B dose rate to the expected dose rate based on the beam-counting scintillator, and tests using the flight spare have yielded the expected results.

The accuracy of the dose rates depends directly on the accuracy of the energy calibrations of B and E, as well as RAD's highly accurate internal measurements of detector livetime and precise knowledge of the detector masses, which are straightforward to compute. Lastly, it is also necessary to account for the RTG contributions to the observed dose rates. Data obtained after integration of the RTG on Curiosity, but prior to launch, can be used to estimate the necessary corrections.

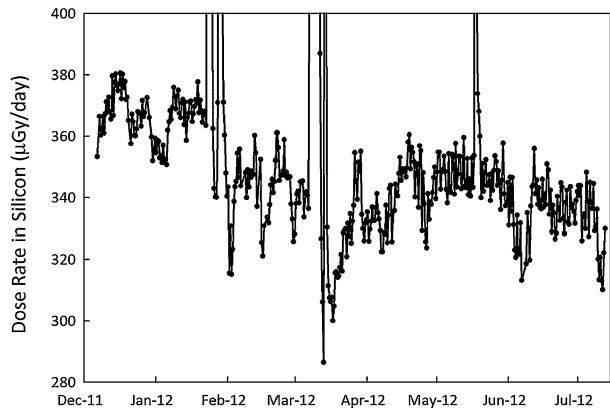
The mass calculations for B and E are trivial: both are hexagonal prisms. E has a depth of 1.8 cm, a surface area of 18.78 cm<sup>2</sup>, and a density of 1.03 g cm<sup>-3</sup>, giving a mass of 34.88 g. The B segment of the diode has a depth of 300 μm, a surface area of 1.92 cm<sup>2</sup>, and a density of 2.33 g cm<sup>-3</sup>, for a mass of 0.1315 g. Because one of the C2 segments surrounds B, particles that hit near the border between the two may produce charge in both segments. It is probably reasonable to assume that the amount of charge that leaks out of B into C2 is balanced by charge that leaks into B from C2.

### 6.5.1 RTG Dose Rates in Ground Testing

RAD was powered on and acquired data for one hour on 20 November, 2011, six days before the MSL spacecraft was launched to Mars. The B dose rate averaged 45 μGy/day, and the E dose rate about 0.4 μGy/day. However, as noted above, at this time the B dosimetry trigger was defined by the BH slow token, with a threshold of 200 keV, well above the  $\Delta E$  from MIPs. The RTG background dose in B appears to largely come from relativistic conversion electrons with energies up to about 6 MeV. This meant that a substantial fraction of the dose was missed by the L2(4) trigger due to the relatively high threshold. Fortunately, those events satisfied the charged-particle triggers L2(0) and L2(1), at least when the electrons were incident on RAD from above and therefore in either the A1 • B or A2 • B angular cone, so we can estimate the effect of the high threshold. Of the events in either cone, the dose associated with those that had the L2(4) trigger set was 52 % of the total. This implies that, had the L2(4) trigger been defined as BU rather than BH, the RTG background would have been estimated to be 84 μGy/day. We have, out of necessity, assumed that the events in the coincidence geometry constitute an unbiased sample, which may not be correct given that the RTG is located to the side of RAD and only slightly above it.

Both of the estimates of the RTG background in B given above are used in the following. The RTG contribution to the E dose rate can be ignored, based on these data. This may seem

**Fig. 5** GCR dose rate in silicon (specifically, the B detector) as measured by RAD during MSL's cruise to Mars in 2011–2012. The RTG background has been subtracted according to the procedures described in the text

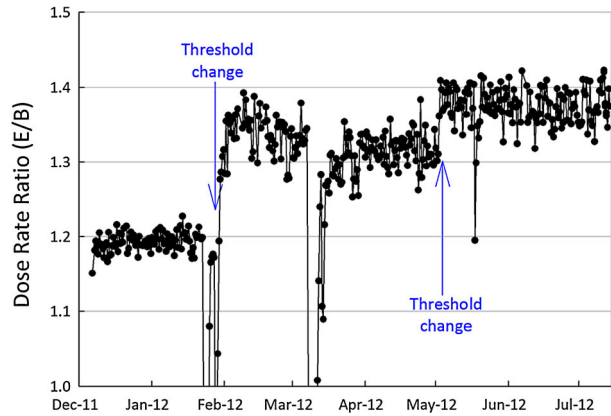


surprising given that the primary emissions from the RTG are neutrons and  $\gamma$ -rays, however as noted above the E thresholds are high. And while the B dose rate from the RTG appears to be dominantly due to electrons, those will not reach E because it is shielded by other detectors ( $12.6 \text{ g cm}^{-2}$  of CsI above,  $1.2 \text{ g cm}^{-2}$  of plastic on all other sides), and electrons at the observed energies do not have sufficient range to penetrate to E.

### 6.5.2 B Dose Rates in Cruise

RAD began data acquisition on 6/12/2011, and operated with no configuration changes until 23/01/2012, 196 days before MSL entered the Martian atmosphere. The average dose rates for this period were found to be  $354 \text{ } \mu\text{Gy/day}$  in B (dose to silicon) and  $432 \text{ } \mu\text{Gy/day}$  in E. Since L2(4) was defined as the BH slow token, the expected RTG contribution to the dose rate in B was  $45 \text{ } \mu\text{Gy/day}$ . On 27/01/2012, a new EVIL table was uploaded to RAD for the primary purpose of lowering the E thresholds; this had no effect on the B dose rate. However, at the same time, a significant solar event was in progress, with a subsequent Forbush decrease observed by RAD, after which the dose rate in B fell to an average of  $332 \text{ } \mu\text{Gy/day}$ . In March 2012, a large solar particle event (SPE) was followed by another Forbush decrease that lasted approximately two weeks before the GCR dose rate in B returned to a rate of about  $343 \text{ } \mu\text{Gy/day}$ . On 11/06/2012, a new EVIL table was uploaded that redefined L2(4) to use the BU slow token instead of BH. As a result, the measured B dose rate increased by  $95 \text{ } \mu\text{Gy/day}$ . (This estimate comes from comparing data from 28/05/2012 to 03/06/2012 with data from 13/06/2012 to 19/06/2012. The date ranges were chosen because during these periods the average dose rates in E were equal to within better than 1 %; the intent is to remove effects of small changes in solar modulation on the B dose rate.) Based on the analysis of RTG data presented above, we estimate that  $39 \text{ } \mu\text{Gy/day}$  of this increase came from increased RTG background admitted due to the lower threshold, while the remaining  $56 \text{ } \mu\text{Gy/day}$  comes from the inclusion of MIPs that had previously not been counted in the B dose rate. If we add the  $56 \text{ } \mu\text{Gy/day}$  MIP contribution to the dose rate recorded prior to the configuration change, it is partially offset by the  $45 \text{ } \mu\text{Gy/day}$  RTG background correction that is applicable for the earlier period. To a good approximation, then, dose rates recorded in B prior to the configuration change should have  $11 \text{ } \mu\text{Gy/day}$  added, and the dose rates after the change should have  $84 \text{ } \mu\text{Gy/day}$  subtracted. Figure 5 shows the B dose rate data for GCRs combined in this way, with twelve-hour averaging. (SPE data have mostly been removed by requiring the B dose rate to have been less than  $500 \text{ } \mu\text{Gy/day}$  in this figure.) The

**Fig. 6** Ratio of E dose rate to B dose rate, reflecting changes made to E thresholds on 27/01/2012 and 02/05/2012. The ratio is sensitive to details of the radiation environment, as can be seen from the small change before and after the large SPE of early March 2012



data before and after the configuration change appear to smoothly join, and show an overall decreasing trend, consistent with the general trend of increasing solar modulation during this period.

### 6.5.3 E Dose Rate in Cruise

The E thresholds were reduced on 27/01/2012 23:34 UTC, which by happenstance was during a significant SPE. As shown for the B detector above, the GCR dose rate decreased after the event due to a Forbush decrease, but the measured E dose rate increased at this time due to the threshold reduction. A straightforward way to assess the effect of the threshold change is to examine the ratio of dose rates in E and B, as shown in Fig. 6. The B dose rate has been corrected for the RTG background as per the preceding. During the SPEs in late January and early March, the ratio dropped considerably because the low-energy protons did not reach E, and thus the B dose rate has a large increase relative to the increase in the E dose rate, causing the ratio to fall. Comparing quiet periods, it can be seen that the ratio changed from an average of 1.19 before the threshold adjustment to about 1.35 immediately afterwards. The ratio dropped slightly after the next large SPE in early March 2012, likely indicating the lingering effects of that event on the GCR environment. On 02/05/2012 22:32, a new EVIL table went into effect with slightly lowered E thresholds. The ratio then rose to an average of about 1.38. The 11/06/2012 table change described above had no apparent effect on the dose rate ratio, which strongly suggests that our adjustments to the B dose rate are accurate.

### 6.5.4 Surface Dose Rates

RAD was turned off for the final three weeks of the transit to Mars. After the successful landing of Curiosity on the surface, dose rates observed by RAD dropped significantly, which was expected based on the  $2\pi$  shielding provided by the body of the planet and the additional increment of shielding provided by the atmosphere compared to the shielding during cruise. If we apply the same RTG background correction to the B dose rate that was appropriate for the data taken after the 11/06/2012 table update, the ratio of E to B dose rates averages 1.55 in the early surface mission, compared to 1.37 late in cruise. There were no changes in the relevant thresholds during this period. The cruise data following the March 2012 SPE show definitively that the dose rate ratio is sensitive to the environment,

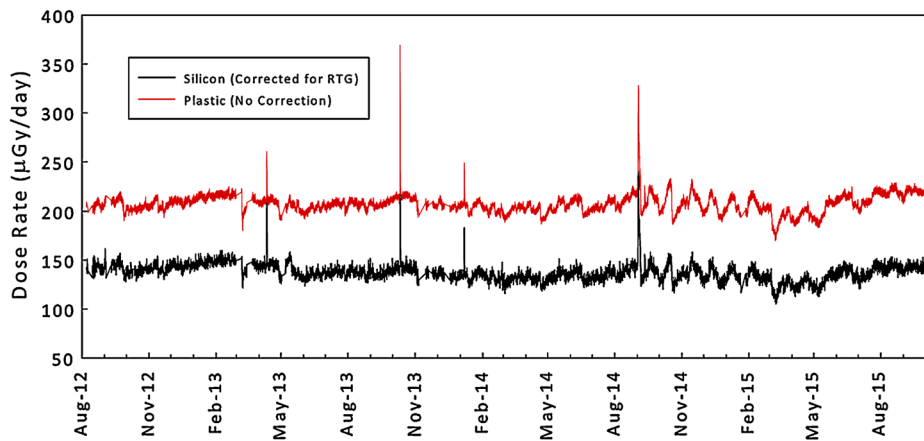


**Fig. 7** Dose rates in the B and E detectors, with the former corrected for RTG background

so it is conceivable that the observed 15 % increase in the ratio merely reflects a changed external environment, that hypothetically could be caused by a large neutron dose on the surface that was not present in space. However, careful analysis indicates this is likely not the case (Köhler et al. 2014, 2015). A far more likely reason for the difference is that the descent vehicle that was located directly above RAD during the trip to Mars is not present on the surface. The descent vehicle was almost certainly a secondary source of some of the RTG background observed before launch and in cruise, as high-energy  $\gamma$ -rays could pair produce in it, and neutrons could undergo both elastic and inelastic interactions in it, leading to the observed flux of energetic electrons in B. There is no direct way to separate the contributions of the ambient environment on the surface of Mars from those of the RTG, but we can estimate the difference in the RTG background by noting that changing the estimated background dose rate from 84 to 66  $\mu\text{Gy/day}$  causes the E to B dose rate ratio to return to the value of 1.37 found in data from late in cruise with the same threshold settings. Allowing for the possibility that some of the change in the dose rate ratio is due to real environmental differences, it is reasonable to use the midpoint of the two background dose rate values with an uncertainty large enough to cover both, namely  $75 \pm 9 \mu\text{Gy/day}$ .

Figure 7 shows the E and B dose rates for the surface mission, with this correction to the B dose rate and no correction to the E dose rate. Only a few modest SPEs have been observed, owing to the unusually weak solar maximum of Solar Cycle 24, and to the shielding provided by the atmosphere above RAD. A number of Forbush decreases have been observed, as well as periodic variations starting in late 2014 that are clearly linked to solar rotation.

## 6.6 Updated Calibration

In the course of this work, a careful re-analysis of calibration using surface data was performed. The previous calibration using MIP peaks and bootstrapping was performed in January 2012, and the onboard calibration parameters have been essentially unchanged since then. Drifts of pedestals and gains are possible, and it is also the case that the temperatures under which the detectors and electronics operate on Mars are significantly lower than in cruise, with wide diurnal swings. Data acquired during the first month of cruise were used for the original calibration, and temperatures inside the REB were always in a narrow range

from 28 °C to 35 °C, with an average temperature of 33 °C. On the Martian surface, temperatures in the REB have varied from 9 °C to 39 °C, with an average of 18 °C. Furthermore, early in cruise, we had not enabled the onboard temperature compensation tables (described in Appendix E), which were enabled later in cruise and which have been used almost continuously on the surface.

As explained in the preceding, accurate calibration is most essential for the B and E channels that feed directly into the dosimetry results. Analysis of the surface data showed that a change of +2 % to the inverse gain factor used in the EVIL table was needed for the BU channel, with −5 % changes needed for the remainder of the B channels. The changes were implemented starting on 10 March 2016, and (as expected) caused the measured B dose rate to increase by about 1.5 % compared to the calibration used previously. In Zeitlin et al. (2013), we estimated the uncertainty in the B dose rate due to calibration uncertainties to be  $\pm 7$  %, far larger than this change. Since the GCR dose rate in B has been in the range from 120 to 170  $\mu\text{Gy/day}$  during the surface mission, the  $\pm 9$   $\mu\text{Gy/day}$  uncertainty in the RTG background correction is now dominant, so that  $\pm 7$  % remains a conservative estimate of the overall uncertainty in the B dose rate. We are also interested in measuring the dose equivalent, which, in conventional dosimetry, is directly related to radiation-induced cancer risk. Dose equivalent depends on the average quality factor,  $\langle Q \rangle$ , which in turn depends on the linear energy transfer (LET) spectrum in water (International Commission on Radiological Protection 1991). To estimate this, the spectrum of  $dE/dx$  in silicon—specifically, that in B using A2 • B coincidence events—is scaled by a constant factor to LET in water. Using a constant is a reasonable approximation, but is not formally correct, and introduces uncertainty in the estimate of  $\langle Q \rangle$ , which is accounted for in our published results.  $\langle Q \rangle$  was found to be  $3.8 \pm 0.3$  in cruise (Zeitlin et al. 2013; Schwadron et al. 2014) and  $3.1 \pm 0.3$  on the surface (Hassler et al. 2014). The small changes in B calibration found here do not change these  $\langle Q \rangle$  values beyond the stated uncertainties.

For the EH channel, no significant difference in gain was seen in comparing the surface data to cruise data, but for EI, EN, and EL we find a differences of 10 %, 5 %, and 15 % respectively. The net effect of these changes (also implemented on 10 March 2016) reduced the E dose rate by about 4 %. In previous publications that used the E dose rate (Zeitlin et al. 2013; Hassler et al. 2014), we estimated 15–20 % uncertainties, so this revision falls well within the previously stated error bar.

Changes to other channels are mostly on the order of 5 % or less, and are expected to have no practical impact on any results. We expect to update the onboard calibration parameters in early 2016.

## 7 Conclusions

The RAD instrument has operated successfully on the surface of Mars for over 1400 sols at the time of this writing. Calibration of the instrument includes both the conversion of digitized pulse heights to deposited energy values and the determination of thresholds, with adjustments when needed or desired for particular measurements. All aspects are well understood, and in the course of this work, previously-reported dose rates and related quantities have been verified to be accurate within the stated uncertainties. Proper functioning of the onboard Level 2 and Level 3 firmware, and accurate recording of doses, require that many parameters (fast thresholds, slow thresholds, pedestals, and gains) are set correctly. Rates are dominated by dosimetry triggers in the B and E detectors that require hits only in those

detectors; these events are so numerous that only a small fraction of the pulse-height records can be telemetered to Earth. In contrast, the large majority of charged-particle coincidence events and neutral particle events are stored for telemetry, including all of the heavy-ion coincidence triggers L2(2) and L2(3). Coincidence events are subject to selection criteria applied by the L3 logic, which depend to a large extent on slow thresholds and to a lesser extent on energy calibration. Selection criteria are generally left loose, enabling the maximum throughput of event records for ground analysis.

Observed dose rates have to date been dominated by GCRs. Background from Curiosity's RTG power source has been accounted for using data obtained before launch and a conservative estimate of the uncertainty caused by the changed configuration of the rover from cruise to the surface mission.

Recent changes include improved flight software, with version 2.7 having been activated in late 2015, and implementation of a dedicated Level 2 trigger to look for signatures associated with radon in the Martian atmosphere. Future plans include a campaign to gradually reduce thresholds for neutron detection as low as possible without incurring excessive background rates from the RTG.

**Acknowledgements** RAD is supported by NASA (HEOMD) under JPL subcontract #1273039 to Southwest Research Institute and in Germany by DLR and DLR's Space Administration grant numbers 50QM0501 and 50 QM1201 to the Christian Albrechts University, Kiel. Part of this research was carried out at the Jet Propulsion Laboratory, California Institute of Technology, under a contract with the National Aeronautics and Space Administration.

## Appendix A: Detector Energy Calculations

RAD contains multiple readout channels for each detector, with a range of gains designed to accommodate the wide range of  $\Delta E$  encountered in the space radiation environment. In L2 processing, several modes are available for combining channels to yield a single  $\Delta E$  reading for each detector. These "detector energies" are used by the algorithms in L3 for event categorization, selection, and assignment of storage priority. To date, only two modes of combining channels have been employed. The first is the simplest—the highest-gain channel that is not in or near electronic saturation is used. This mode ("mode 0") is used for A1, A2, B, C, and C2. For the F1 and F2 detectors, to date only one readout channel of each has been used, so there is no ambiguity. For the D and E detectors, we read up to four channels each per event. These are combined according to the L2 "mode 1" algorithm, which makes use of as many channels as is sensible. The algorithm discards channels with either too low an ADC reading (near or in the electronic noise) or too high a reading (near or in saturation). Since most events have small energy depositions, the energies found in the two highest-gain channels, DH and DI for D and EH and EI for E, are typically averaged to arrive at the detector energy. Since these channels are on different readout diodes, the position dependence of the energy readings is smoothed out, improving the  $\Delta E$  resolution compared to using only a single channel. (This is why EH and EI have been adjusted to have nearly equal overall gains, as have DH and DI.) This approach thus tends to compensate for the intrinsic position dependence of the scintillation light output. In many cases, all three diodes can contribute a signal to the energy determination, further improving resolution. When three channels have signals in their usable ranges, all are combined, with the two lowest-gain channels receiving weights of 0.25 and the highest-gain channel a weight of 0.5. When four channels can be used, the two with the lowest gains each get weights of 0.125, the channel with the second-highest gain gets weight 0.25, and the highest-gain channel gets



**Table 6** Dosimetry histograms

Category	X-axis quantity	# of $x$ bins	Y-axis quantity
Energy in B, binned by time	Interval number	16	Summed energy in B
Energy in E, binned by time	Interval number	16	Summed energy in E
Energy in B, binned by B energy	Energy in B	16 (64)	Summed energy in B
Energy in E, binned by E energy	Energy in E	16 (64)	Summed energy in E
Energy in B for A1 • B coincidences	Energy in B	44 (52)	# of events
Energy in B for A2 • B coincidences	Energy in B	44 (52)	# of events

weight 0.5. On heavy-ion events with large energy depositions, it is typically the case that only the low-gain channels (DL, EL and in some cases EN) are not in saturation and are the only channels used for the energy calculation.

## Appendix B: L3 Histograms

### B.1 Dosimetry Processing

Table 6 lists the L3 dosimetry histograms. The first two are essentially running sums of all energy depositions above threshold in the B and E detectors, with 16 bins per histogram. With the usual 16-minute observing period, each bin corresponds to one minute. When RAD Flight Software was updated from version 2.6 to 2.7 on sol 1142 (UTC 23/10/2015 9:14), the number of bins in the coincidence histograms was increased from 44 to 52. Because the data are binned logarithmically with base 2, with four bins per octave, these histograms now cover a dynamic range of  $2^{13}$  as opposed to  $2^{11}$ . Also under FSW version 2.7, the number of bins in the energy histograms was increased from 16 to 64. Additional details of the FSW upgrades are provided in Appendix F.

Unlike the data processing for other histogram categories, dosimetry processing does not make any assignments of PHA storage priority. There are simple cuts for the time and energy histograms built into the software, which can be used to require that the energy depositions are above noise, or some other threshold if desired. These cuts are in practice not needed since the slow tokens provide the same functionality, and the cut values, which are configurable, are set to 0 in the setup table. For the LET histograms, events are only entered if the energy deposits in A and B are mutually consistent to within a factor of 4. In principle, this cut is also configurable, but in practice it has been constant. It is deliberately kept loose to allow for events to pass even if one energy reading or the other is in the high-end tail of the  $\Delta E$  distribution. These “Vavilov tails” are populated by high-energy particles.

### B.2 Charged Particle Processing

As can be seen in Figs. 3 and 4 of the main text, and in Ehresmann et al. (2014) as well, RAD is capable of identifying charged particles, particularly those with low enough energy to stop in the detector stack. The onboard charged particle histograms, detailed in Table 7, were designed to make use of these capabilities. As explained in Hassler et al. (2012), the quantity on the  $y$  axis of the stopping particle histograms represents, approximately, the



**Table 7** Charged particle histograms

Category	$x$ -axis quantity	# of $x$ bins	$y$ -axis quantity	# of $y$ bins
Stopping	$\log_2(E_{\text{tot}}/E_{\text{ABC}})$	16	$\log_2(E_{\text{tot}} \times E_{\text{ABC}})$	12
Penetrating	$\log_2(E_{\text{ABC}})$	24	$\log_2(\text{energy in } E) - \log_2(E_{\text{ABC}})$	3

Note:  $E_{\text{ABC}}$  = sum of  $\Delta E$  in A, B, and C,  $E_{\text{tot}}$  = sum of  $\Delta E$  in A, B, C, D, E

charge of the incident particle, while the  $x$  axis quantity is roughly proportional to the incident energy. For the lightest ions, separation of isotopes is also clearly seen in this histogram, which is, roughly speaking, a rotation and orthogonalization of the scatter plots in the upper right-hand corners of Figs. 3 and 4. Since penetrating particles by definition only deposit a fraction (often very small) of their energy in the detectors, it is more challenging to extract information about them. When highly relativistic particles traverse the detector stack, their  $dE/dx$  remains nearly constant, and these particles populate a narrow band in  $y$  in the penetrating particle histogram, with separation along the  $x$  axis according to  $\log(Z^2)$ . This is why there are many more  $x$  bins than  $y$  bins.

Detailed maps of the charges and energies that correspond to particular histogram bins are complex, and are beyond the scope of this article. They are available from the authors upon request for those wishing to do their own detailed analysis of RAD PHA data using the publicly-available Planetary Data System archive.

### B.2.1 Selection of Low-Priority Events

Low-priority charged particle events satisfy the L2(0) or L2(1) triggers that require hits in A1U or A2U and BU. These are low- $Z$ , low-LET events, and they are common; these two triggers have a combined rate of about 0.7 to 0.8 Hz in solar quiet time. Charged particles with low hardware priority will populate the corresponding penetrating histogram if the C, D, E, and F2 detectors each have at least one slow token set among their readout channels. If one or more of these detectors does not have a slow token set, the L3 logic as presently configured treats the event as a stopping charged particle. An option is built into the stopping-particle logic to make a cut requiring that the energy deposition in F1 is less than a preset value, and optionally for F2 as well. At present these cuts are effectively disabled by setting the cut values to the maximum possible value, so that they are never exceeded. The stopping particle logic was slightly different under FSW 2.5, using F1 and F2 slow tokens instead of energy values. This would have caused some valid events to be lost if the slow thresholds had been set to be in the noise, as is desirable for their use in neutral particle detection. (See Appendix D for details.)

### B.2.2 Selection of High-Priority Events

The L3 logic for penetrating charged particles with high priority (that is, coming in under L2 triggers 2 or 3) inspects several energy deposition ratios to verify that  $dE/dx$  stays reasonably constant through the stack. A cut is also made on the energy deposited in the C2 (anticoincidence) detector. High-priority events with stopping particles are also subject to a number of cuts, which (similar to the penetrating particle cuts) depend on energy deposition ratios. Exactly which ratios are checked depends upon where the particle appears to have stopped. All cuts are kept loose, but—as noted in Sect. 3 above—even if events fail one or more cuts, they are assigned the highest storage priority, 3, by the catchall in the logic.

**Table 8** Neutral particle histograms

Histogram	x-axis quantity	# of x bins	y-axis quantity	# of y bins
Neutral particles (2-d)	$\log_2(\text{energy in E})$	8	$\log_2(\text{energy in D})$	8
Neutral particles, D energy	$\log_2(\text{energy in D})$	48 (96)	# events	n/a
Neutral particles, E energy	$\log_2(\text{energy in E})$	48 (96)	# events	n/a

Note: The number of bins in the one-dimensional histograms was 48 under FSW versions 2.6 and earlier, and 96 under version 2.7

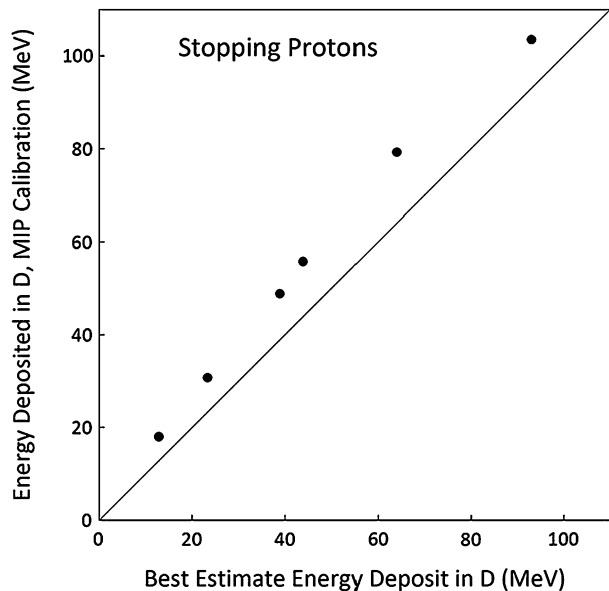
### B.3 Neutral Particle Processing

Table 8 shows the three types of histograms are defined for neutral particle processing: simple one-dimensional histograms of the energy depositions in the D and E detectors, and a two-dimensional histogram with very coarse binning for relatively rare neutral-particle events with a D • E coincidence (L2 trigger 8). Events in this category are given high hardware priority in L2, but because they are not selected in the configurable L3 logic catchall, their storage priorities are assigned by the two-dimensional histogram if they pass cuts, which consist of checks on the energy deposits in the F1, F2, and C2 anticoincidence detectors, as well as in the C detector. A careful recent study shows that the F1 and F2 cuts are overly restrictive and lead to about two-thirds of these triggers failing cuts and being assigned storage priority 0. All events that satisfy only L2(7) (D neutral), or that satisfy a combination of L2(5) (E dosimetry) and L2(6) (E neutral), also receive storage priority 0. In the present configuration, only about 1 % of these events are telemetered to Earth, but even so, a reasonable statistical sample of these events can be gathered because they are relatively common. It is likely that a revised Setup table, with looser cuts on F1 and F2 energies, will be uploaded to RAD in early 2016.

## Appendix C: CsI Light Output for Stopping Particles

As discussed in Sect. 6, and shown in Figs. 3 and 4, charged particles that stop in the D or E detectors are assigned energies that are slightly off from the correct values. This is a consequence of using MIPs to set the gain parameters for the D and E channels, because penetrating and stopping particles have different calibrations. Birks' formula (Birks 1964) is often used to describe the non-linearity of scintillator light output as a function of energy deposition, and it predicts that stopping protons should give less light output than penetrating protons. The results in Sect. 6 for stopping particles go in the opposite direction from this prediction, while penetrating heavy ions show the expected behavior (i.e., less light output than would be obtained if the response were linear with  $\Delta E$ ). Results similar to ours can be found in the literature. In particular, in Figs. 3–6 of Koba et al. (2011), Koba et al. aggregate published results for light outputs of CsI(Tl) and other inorganic scintillators relative to outputs from  $^{137}\text{Cs}$   $\gamma$ -rays as a function of  $dE/dx$ . Birks' formula predicts that so-called "scintillation efficiency" is less than 1, and data for the other scintillators shown in these figures—NaI(Tl), GSO(Ce), and LYSO(Ce)—are consistent with this behavior. However, several CsI(Tl) data points have measured efficiencies greater than 1, going as high as 1.4, and several other points have efficiency less than 1 but well above the predictions of Birks' formula. It was noted by Murray and Meyer (Novak et al. 2012) that light output for electrons (and presumably other sparsely-ionizing particles such as the MIP protons used to calibrate

**Fig. 8** Measured energy depositions in D using MIP calibration to set the energy scale (y-axis), vs. calculated energy deposition, obtained with the flight spare RAD in various proton beams. Similar to the flight data, stopping protons over this energy range yield more light than expected based on the calibration method



RAD) in inorganic scintillators is suppressed by recombination effects. In view of these observations, it is perhaps not surprising that the light yield for stopping protons in RAD data is higher than we would expect from MIP calibration and Birks' formula.

To verify that there is not some unexpected problem with the calibration of the flight unit, we undertook a careful study of proton and helium beam data acquired with the flight spare unit at the National Institute of Radiological Science in Chiba, Japan. Both the cyclotron and HIMAC facilities were used. At HIMAC, the instrument was placed in beams of protons at 160 MeV and  $^4\text{He}$  at 180 MeV/nuc. Moderators were placed in the proton beam to reduce the energy incident on RAD to about 96 MeV, and later to about 71 MeV. All four of these data sets were used, in conjunction with detailed energy loss calculations, to perform calibration of the A2U, BU, and CU channels; we estimate the resulting parameters are accurate to better than 2 %. Calibration parameters were also obtained for the DH channel separately, using muon data acquired in sporadic runs, typically 12–16 hours in duration, that were performed over a period of months. This method yields a gain that agrees with that of DH in the flight unit to better than 8 %.

The data from the NIRS cyclotron were then used for a definitive test of the D calibration for stopping protons. Three beam energies were used, 30, 50, and 70 MeV. With both the 30 and 50 MeV beams, two data sets were taken, one with a 3 mm thick plastic scintillator in the beam ahead of the RAD flight spare, and one without. With the 70 MeV beam, data were only acquired with the scintillator in the path of the beam. The calibrations for A2, B, and C were used in conjunction with energy loss calculations to predict the true energy deposits in D for the five runs. A sixth point was added using HIMAC data in which the nominal 160 MeV proton beam was moderated down to an incident energy estimated at 94.6 MeV. In this case, the protons stop after traversing almost the full depth of D, depositing 93 MeV, very close to the theoretical maximum of 94.8 MeV (which, for normally-incident protons, can be deposited by particles with initial energies of 96.6 MeV). Figure 8 shows the results of the measurements compared to the calculations. In all cases, the calibrated energy deposit is substantially larger than the expected energy deposit based on our calculations (which are

tuned to agree with the measured energy deposits in A2, B, and C). The discrepancies range from nearly 40 % at the lowest energy to 11 % at the highest. The best-fit line through the points, forced through 0, has a slope of 1.18, which should be compared to the approximately 15 % discrepancy seen in the flight data between reported and actual energies in D. We conclude that these results are entirely consistent with the flight data, and also with the results for CsI(Tl) shown in Koba et al. (2011).

## Appendix D: Anticoincidence Thresholds

Another significant change in calibration concerns the slow trigger thresholds for the F1H and F2H channels. Our strategy has been to set these thresholds to be in the middle of the noise peaks of the respective channels. The reason for doing so is that the MIP distributions slightly overlap the noise distributions in these channels. The F1H and F2H slow tokens are crucial components of the anticoincidence logic: if there is significant  $\Delta E$  in either, an event is not considered a possible neutral-particle event. The difficulty lies in defining “significant  $\Delta E$ ” when the noise peak and MIP peak overlap. The approach employed from sol 275 (UTC 22/05/2013 18:06) onward is safe in that it guarantees clean samples of neutral-particle events, since the upper half of the noise distribution, along with any contamination from charged particles, is discarded. The downside is a loss of statistical power, as throwing out half the noise distribution in both F1 and F2 causes RAD to only count one-fourth of valid neutral particle events. However, this is easily mitigated in offline analysis—we simply correct the neutral particle count rates by multiplying in a factor of 4. This factor of 4 reduction in the number of events only increases statistical uncertainty by a factor of 2 (i.e., by  $\sqrt{N}$ ). Figure 9 shows the noise distributions after the most recent tweaks, for events on which either the L2(6) or L2(7) pattern was matched, i.e., an E neutral or D neutral event. Best fits to (expected) normal distributions are also shown, along with the fit parameters. Our intent in adjusting the thresholds for these channels is to put them at the center of the noise peaks, which are intended to be at 250 ADC counts; the fits show that the centroids are very close to the desired values, and both distributions are consistent with normal distributions based on the  $\chi^2$  values.

## Appendix E: Temperature Compensation Tables

On the Martian surface, temperatures in the REB have averaged 18 °C, and stayed in the range from 9 °C to 39 °C. In Hassler et al. (2012), we presented inverse-gain data taken during thermal-vacuum testing for the A1U, A2U, BU, and CU readout channels (Fig. 15b). Data from these four channels follow the same trend when plotted relative to the values obtained at 0 °C, and a single fit to a third-order polynomial suffices to describe the temperature dependence. Because the energy required to create an electron/hole pair in silicon is very nearly independent of temperature, any functional dependence of the system response can safely be assumed to be caused by the electronics. Applying the fit parameters from these data to the temperature range experienced on Mars, we find expected gain variations of less than  $\pm 1$  % relative to the value at 10 °C. There are, accordingly, no temperature-dependent gain corrections applied onboard. Corrections are applied for fast thresholds, slow thresholds, and pedestal shifts due to temperature variations.

As described in Hassler et al. (2012), eight configurable temperature compensation tables are stored in the RAD firmware. An operating range of  $-20$  °C to  $+55$  °C was anticipated,

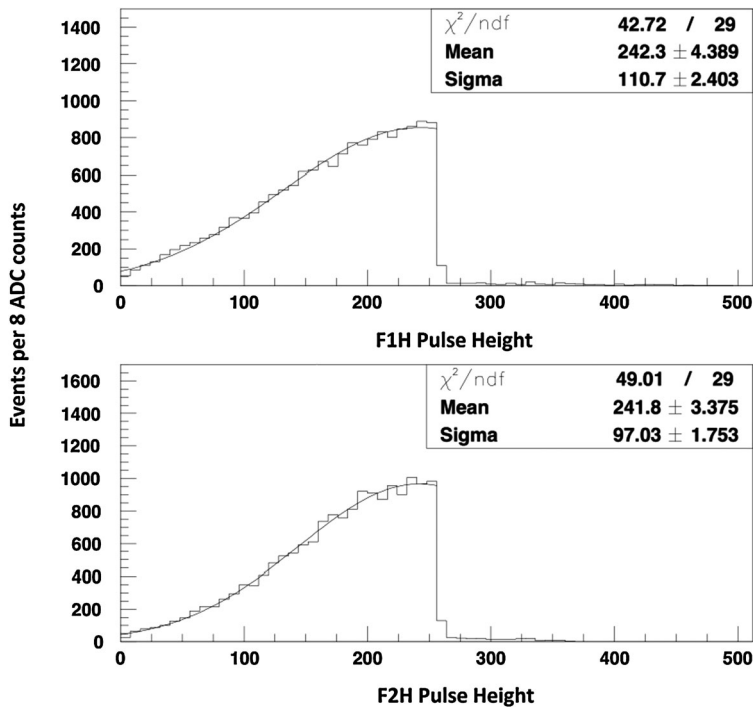


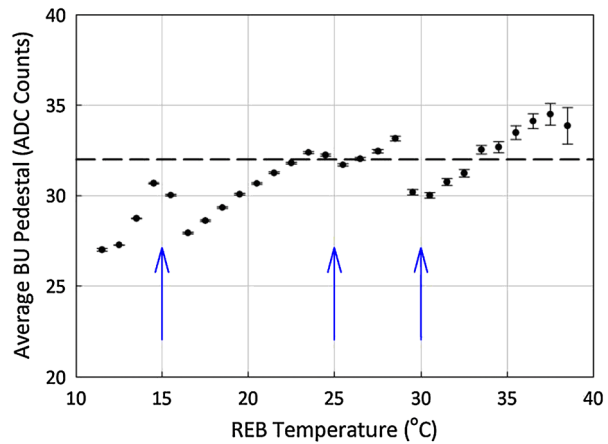
**Fig. 9** Histograms of the F1H and F2H pulse height distribution on neutral particle events. By definition, on these events the corresponding slow tokens are not set. The thresholds are intentionally set to fall at the mid-points of the noise distributions, so that the neutral particle histograms contain clean samples, at the cost of a net factor of four in efficiency

and the onboard tables cover this range, but because the actual operating range is narrower, not all the tables are used. When RAD begins an observation, it takes a reading from one of the four thermistors distributed throughout the unit (we opt to use one in the REB), and based on that reading, the L2 firmware implements the compensation table that best corresponds to the measured temperature. Each compensation table provides “deltas,” that is, generally small modifications that are applied by L2 to the nominal values taken from the EVIL table.

On a typical sol, two to four compensation tables are used. Data to populate the tables were obtained in standalone thermal-vacuum testing of RAD prior to delivery, and during similar testing performed on the Curiosity rover after integration (Schwadron et al. 2014). Additional refinements to pedestals were made based on data obtained over the first 300 sols on Mars; revised compensation tables went into effect on sol 384 (UTC 4/09/2013 14:44). Over the full temperature range, the large majority of pedestal adjustments are less than  $\pm 10$  ADC counts from the nominal pedestals, which are typically around 1600 ADC counts. The largest deltas from one temperature extreme to the other approach 40 ADC counts, and are for non-critical channels (A1L, CM, CL, DL, and A1H which is not part of any L2 readout mask).

The BU channel has a relatively large pedestal adjustment, 28 ADC counts over the full range, and data from this channel are used to illustrate the compensation method and its effects in Fig. 10. On the y axis, we plot the average BU pedestal, which ideally would be at a constant value of 32 as indicated by the dashed line, versus temperature as measured in the REB. The actual average of the data is 30 ADC counts, indicating that an overall upward

**Fig. 10** Behavior of (compensated) BU pedestal as a function of temperature, for MSL sols 600–1100 (UTC 14/04/2014 01:57 to 9/9/2015 19:22)



adjustment of +2 is needed in the EVIL table. The compensation tables are organized so that all adjustments are relative to the settings that are appropriate for 20 °C, based on pre-flight data, and ranges are as indicated by the blue arrows in the figure. That is, if the pre-observation temperature is between 10 °C and 15 °C, a particular table is used; a different is table is used from 15 °C to 25 °C, etc. At the lowest temperatures shown, a delta of −12 ADC counts is applied; in the next range, the delta is −4, then 0, then +7. Within the range of a particular table, there is dependence on temperature, e.g., in going from 16.5 °C to 24.5 °C, the average pedestal value rises from 28 to 32 ADC counts, or 0.5 ADC count per degree Celsius. The trends here show that the tables for the two lowest temperature ranges need slight upward adjustments of 2 or 3 ADC counts for BU, while the table for the highest temperature range needs an adjustment of about 3 ADC counts in the other direction. In examining this figure, it should be kept in mind that one ADC count in this channel corresponds to an energy deposition of about 320 eV, so that the adjustments discussed here amount to energy changes of less than 1 keV, roughly 1 % of the energy deposited by a MIP.

As noted in the main text, fast tokens are enabled only for three channels (BU, DH, and EH). For BU, the adjustment corresponds to  $\pm 3.5$  keV relative to the nominal threshold, which is set at about 30 keV, well below the minimum level of 60 keV required to record all MIPs. The DH adjustment is negligible, and EH requires no adjustment. Slow threshold adjustments are also negligible, with two exceptions—DI which is raised by  $\sim 2$  MeV when warmest, and decreased by a similar amount when coldest, and C2H (an anticoincidence channel), which is reduced by about 40 keV at the coldest temperatures.

On the whole, RAD's temperature compensation capabilities are valuable, but play less of a role than was originally envisioned. There are two reasons for this. First, RAD is attached to Curiosity's Rover Avionics Mounting Platform (RAMP), which moderates temperatures. Second, RAD stays relatively warm because it is powered on, in data acquisition mode, almost continuously, in contrast to initial plans that called for an operating cadence of 15 minutes per hour with 45 minutes per hour powered off.

## Appendix F: Flight Software Updates

At launch, the Flight Software version was 2.5, reflecting a number of iterations that had been performed during development and testing. Analysis of cruise data revealed a

**Table 9** Changes in Flight Software version 2.6

Change	Explanation
Add code to avoid watchdog timer expiration during shutdown.	During the shutdown process following an observation, a timer checks to make sure the process is not hung. Under FSW version 2.5, the timer was observed to expire even when there was no problem with the shutdown process, causing loss of some observation packets. Extra calls to “kick” the timer were added to avoid this condition, and no subsequent data losses have been seen.
Bug in B dosimetry fixed.	A code bug caused the low-priority B dose vs. B energy data to be stored in both the low- and high-priority histograms. This is inconsequential since these histograms have not been (and are unlikely to be) used for data analysis.
Detector select mask was read incorrectly in L3.	An array used in Level 3 contains a bit mask showing which readout channels are selected for use in Level 2. (There is a down-select from the 36 VIRENA channels to a maximum of 32 in L2.) Ground testing showed that the array was being read back-to-front instead of front-to-back. This has been successfully worked around by keeping the mask symmetric, i.e., the 32 channels selected in all EVIL tables used to date form a bit mask with hexadecimal value 0x3FFFFFFC. Keeping the mask symmetric is not required in FSW 2.6 and later, but it has not been changed from this value.
Fast token mask added to readout of PHA events.	Previously we had no knowledge of which fast token or tokens initiated an event.
Neutral histogram logic.	Use F1 and F2 energy readings rather than slow token values.
Penetrating charged particle histogram logic.	Remove check on F1 from logic; cut on ratio of E detector energy to $E_{ABC}$ instead of cutting on $E_{tot}$ .
Stopping charged particle histogram logic.	Remove cuts on F1 and F2 slow tokens, replace with cuts on F1 and F2 energy values.

previously-unnoticed problem with the logic in the L3 data analysis firmware: One of the event selection cuts for penetrating heavy-ion events required  $\Delta E$  in F1 to be small. However, sharing of scintillation light with F2 produces signals in F1, so that heavy-ion events failed the cut and were discarded rather than being stored in the PHA event buffers. Because the dosimetry processing in L3 occurs before any other logic is applied, these events did contribute to the measured dose rates, so in that sense they were not lost, but they were not present in the PHA data that were stored and telemetered to Earth. To work around the problem, the F1 calibration gain was set to 0 in the 11 June 2012 EVIL table update, so that all events would (and did) pass this cut. The longer-term solution to the problem was to remove this particular selection cut from the firmware; that change was implemented as part of the RAD FSW 2.6 update, which went into effect on sol 404.5 of the surface mission (UTC 24/01/2014, 09:32). Other small improvements were also incorporated into the update. At the time of the FSW update, a new EVIL table was also loaded into RAD, with the F1 calibration restored to nominal. A full list of the changes in FSW 2.6 compared to 2.5 is given in Table 9.

FSW version 2.6 was successfully uploaded to RAD on sol 404 (UTC 24/01/2014 09:32) of the surface mission, and was in continuous use until sol 1120 (UTC 05/10/2015 15:06), when version 2.7 was uploaded with the goal of improving science data processing. An unanticipated problem with v. 2.7 was encountered within a few days, requiring a temporary rollback to v. 2.6 on sol 1127 (UTC 08/10/2015 01:15). A workaround for the problem was



**Table 10** Changes in Flight Software version 2.7

Increase dynamic range of onboard LET histograms.	In FSW versions 2.6 and earlier, the LET histograms for A • B coincidence events spanned a dynamic range of $2^{11}$ , with 4 bins per octave (44 bins total). This was increased to a dynamic range of $2^{13}$ (52 bins total) in version 2.7.
Increase resolution of neutral particle histograms.	The number of bins in the neutral particle one-dimensional histograms was increased from 48 to 96 under version 2.7.
Add counter for occurrences of Fast Triggers for which no L2 match is found.	It is common for RAD to have a fast trigger—typically due to a $\gamma$ -ray from the RTG directly hitting the DH or EH readout diode—which has no L2 match (i.e., no slow trigger). Such events have no readout, but increment the PHA storage priority 0 counter. This can lead to incorrect normalization in ground analysis of data that makes use of priority 0 data. In version 2.7, an additional counter was implemented so that we have knowledge of the number of events with no L2 match; this number must be subtracted from the total count of storage priority 0 events in order to properly normalize the data.
Add capability to assign separate telemetry downlink priorities for the “extra PHA” packet when it is enabled.	This is an internal parameter used to communicate the telemetry priority of a data product to the rover computer. There are two types of science data products, regular and high-priority, the latter label meant to indicate SPE data. When the extra PHA packet was enabled under version 2.6, both science data products had the same telemetry priority. Under 2.7, the data product with counter data, histograms, and housekeeping information is tagged as high priority while the product with the additional PHA events is tagged as regular priority.

found, and use of version 2.7 resumed on sol 1142 (UTC 23/10/2015 09:14). Version 2.7 provides several minor improvements in the onboard L3 processing, as shown in Table 10.

## References

- H. Bichsel, Straggling in thin silicon detectors. *Rev. Mod. Phys.* **60**(3), 663 (1988)
- J.B. Birks, *The Theory and Practice of Scintillation Counting*. International Series of Monographs on Electronics and Instrumentation, vol. 27 (1964)
- B. Ehresmann et al., Charged particle spectra obtained with the Mars Science Laboratory Radiation Assessment Detector (MSL/RAD) on the surface of Mars. *J. Geophys. Res., Planets* **119**(3), 468–479 (2014)
- J. Guo et al., Modeling the variations of dose rate measured by RAD during the first MSL Martian year: 2012–2014. *Astrophys. J.* **810**(1), 24 (2015a)
- J. Guo et al., Variations of dose rate observed by MSL/RAD in transit to Mars. *Astron. Astrophys.* **577**, A58 (2015b)
- D.M. Hassler et al., The radiation assessment detector (RAD) investigation. *Space Sci. Rev.* **170**(1–4), 503–558 (2012)
- D.M. Hassler et al., Mars’ surface radiation environment measured with the Mars Science Laboratory’s Curiosity Rover. *Science* **343**(6169), 1244797 (2014)
- International Commission on Radiological Protection, *ICRP Publication 60: 1990 Recommendations of the International Commission on Radiological Protection*, vol. 60 (Elsevier Health Sciences, Amsterdam, 1991)
- Y. Koba et al., Scintillation efficiency of inorganic scintillators for intermediate-energy charged particles. *Progr. Nucl. Sci. Technol.* **1**, 218–221 (2011)
- J. Köhler et al., Inversion of neutron/gamma spectra from scintillator measurements. *Nucl. Instrum. Methods Phys. Res., Sect. B, Beam Interact. Mater. Atoms* **269**(22), 2641–2648 (2011)
- J. Köhler et al., Measurements of the neutron spectrum on the Martian surface with MSL/RAD. *J. Geophys. Res., Planets* **119**(3), 594–603 (2014)
- J. Köhler et al., Measurements of the neutron spectrum in transit to Mars on the Mars Science Laboratory. *Life Sci. Space Res.* **5**, 6–12 (2015)



- M.N. Mazziotta, Electron-hole pair creation energy and Fano factor temperature dependence in silicon. Nucl. Instrum. Methods Phys. Res., Sect. A, Accel. Spectrom. Detect. Assoc. Equip. **584**, 436–439 (2008)
- K.S. Novak et al., Mars Science Laboratory rover system thermal test, in *42nd International Conference on Environmental Systems*, San Diego, California, 15–19 July 2012. Available online at <http://hdl.handle.net/2014/44990>
- K.A. Olive (Particle Data Group), Review of particle physics. Chin. Phys. C **38**(9), 090001 (2014)
- A. Posner et al., The Hohmann–Parker effect measured by the Mars Science Laboratory on the transfer from Earth to Mars: consequences and opportunities. Planet. Space Sci. **89**, 127–139 (2013)
- S.C.R. Rafkin et al., Diurnal variations of energetic particle radiation at the surface of Mars as observed by the Mars Science Laboratory Radiation Assessment Detector. J. Geophys. Res., Planets **119**(6), 1345–1358 (2014)
- N.A. Schwadron et al., Does the worsening galactic cosmic radiation environment observed by CReTER preclude future manned deep space exploration? Space Weather **12**(11), 622–632 (2014)
- R.F. Wimmer-Schweingruber et al., On determining the zenith angle dependence of the Martian radiation environment at Gale Crater altitudes. Geophys. Res. Lett. (2015). doi:[10.1002/2015GL066664](https://doi.org/10.1002/2015GL066664)
- C. Zeitlin et al., Measurements of energetic particle radiation in transit to Mars on the Mars Science Laboratory. Science **340**(6136), 1080–1084 (2013)